Julius-Maximilians-Universität Würzburg
Fakultät für Physik und Astronomie
Lehrstuhl für Astronomie

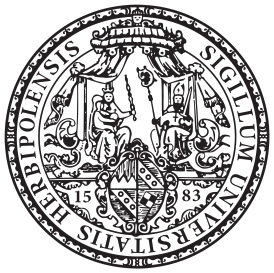

Bachelorthesis

Correlation studies of IceCube neutrinos with subcatalogs of Fermi's 3rd catalog

Autor: Manuel Dörr
Betreuer: Prof. Dr. M. Kadler
Prof. Dr. K. Mannheim
Abgabedatum: 30. August 2016

Zusammenfassung

Diese Arbeit behandelt die Korrelation von kosmischen Neutrinos mit astronomischen Objekten. Hierzu wurde eine 2014 veröffentlichte Liste von 37 hochenergetischen Neutrinos verwendet. Diese wurden mit dem Neutrino Detektor IceCube am Südpol detektiert, welcher mit einem Volumen von $1\,\mathrm{km}^3$ der derzeit größte Neutrinodetektor ist. Diese 37 Neutrinos werden auf ihre Korrelation mit gamma-emittierenden aktiven Galaxienkernen (AGN) getestet. AGN sind kompakte innere Regionen von Galaxien welche enorme Leuchtkräfte aufweisen. Ein Teil der AGN ist in der Lage hochrelativistische Jets auszubilden, welche Emission über das ganze elektromagnetische Spektrum zeigen. In dieser Arbeit wurde die Korrelation zu einer besondere Unterklasse der AGN, den Blazaren, untersucht, welche als aussichtsreiche Neutrino Kandidaten gelten.

Die Algorithmen zur Korrelationsanalyse wurden von T. Glüsenkamp entwickelt und basieren auf der sogenannten "unbinned maximum likelihood" Methode. Die Implementierung dieser Methode wurde in einer vorausgehenden Bachelorarbeit von J. Wiehl erarbeitet. Für die vorliegende Arbeit wurde der Code weiter ausgebaut, wie durch die Implementierung neuer effektiver Flächen oder der Energieabhängigkeit. Hauptsächlich wurde an einem Algorithmus für den Testablauf gearbeitet, welcher den Vergleich von Katalogen unterschiedlicher Größe erlaubt, und am Ende Korrelationswahrscheinlichkeiten für die einzelnen getesteten Kataloge berechnet. Dazu wird die Korrelation eines getesteten Katalogs mit der Korrelation vieler zufälliger Kataloge der gleichen Größe verglichen.

Für diese Arbeit wurden Quellen aus Fermi's 3rd Catalog in die weiteren Klassen BL Lac ähnlicher Objekte (BL Lac), Flach-Spektrum Radioquasare (FSRQ) und Blazar Kandidaten unbestimmten Typs (BCU) unterteilt und getestet. Das Ergebnis zeigte nur für die Klasse der FSRQ eine leichte Korrelation mit einer Signifikanz von $1.39\,\sigma$. Außerdem wurde ein Referenz Katalog erstellt und getestet, welcher neben zufälligen Quellen die Positionen aller Neutrino Ereignisse enthält. Hiermit lässt sich überprüfen, ob die Methodik ausreichend sensibel ist, um die Korrelation festzustellen. Das Resultat zeigte eine Korrelation von $2.92\,\sigma$. Um eindeutigere Ergebnisse liefern zu können, werden in Zukunft Listen mit einer größeren Anzahl an Neutrino Ereignissen verwendet werden.

Abstract

This thesis studies the correlation of cosmic neutrinos with astronomical sources. For this purpose a list of 37 high-energetic neutrino events, published in 2014, was used. These neutrinos were detected by the neutrino detector IceCube, which is located at the South Pole and currently the largest neutrino detector with a volume of $1\,\mathrm{km}^3$. The 37 neutrino events are tested for their correlation with gamma-ray emitting active galactic nuclei (AGN). AGN are compact inner regions of galaxies which are able to emit enormous luminosities. Some AGN produce highly-relativistic outflows, so-called jets, which show emission over the whole electromagnetic spectrum. This thesis studies the correlation of neutrinos with blazars, which are an AGN subclass and belong to the most promising neutrino source candidates.

The algorithm the analysis is based on, was developed by T. Glüsenkamp and is based on a so-called "unbinned maximum likelihood" method. The implementation was done by J. Wiehl in a prior bachelor thesis. For this thesis the code was extended by new effective areas and an energy dependance. The main part was the development of a test procedure, which allows to compare test results from different sized catalogs and calculates a correlation propability for the tested catalog. This is achieved by comparing the result of the tested catalog with results of multiple randomized catalogs of the same size.

In this thesis sources of Fermi's 3rd Catalog were subdivided in BL Lac like objects (BL Lac), flat-spectrum radio quasars (FSRQ) and blazar candidates of uncertain type (BCU). The results only showed a correlation with FSRQ with a significance of $1.39\,\sigma$. Furthermore a reference catalog, which consists of random sources and inserted neutrino positions, was created and tested. With this catalog it is possible to verify, whether the analysis method is sensitive enough to find a correlation. The results showed a correlation of $2.92\,\sigma$. In order to obtain more precise results, lists with more neutrino events will be used in the future.

Contents

1 Introduction

Observations in astronomy are traditionally done with photons. Meanwhile, photons at all energies of the electromagnetic spectrum are used. They are not deflected by magnetic fields, so they point back to their origin. However, above energies of $\sim 100\,\mathrm{TeV}$ the mean free path decreases due to interaction with cosmic microwave background photons (Gould and Schréder, 1966). This fact limits the observation of distant objects at high energies. Observations of comsic rays, which consist mainly of protons, reveal extremely high energies. On the other hand, these charged particles are deflected, for instance by magnetic fields, and therefore provide no information about their origin.

Neutrinos are particles with unique properties. They are neutral like photons, which means they point back to their origin. Furthermore, they are stable and only subject to weak interactions, which allows them to escape dense regions in astrophysical objects and to travel long distances without interaction or absorption. This makes them very interesting to probe the universe at the highest energies and distances.

Because of their unique properties they are hard to detect. It is important to increase the effective volume of neutrino detectors. The neutrino detector IceCube at the South Pole provides an instrumented volume of $1\,\mathrm{km}^3$. Since IceCubes completion it has detected several cosmic neutrinos with energies up to the PeV regime (Aartsen, Ackermann, et al., 2014).

Neutrinos entering the detector can interact with the surrounding ice. Secondary particles like electrons and muons leave characteristic signatures, which are recorded by the detector. Sophisticated Likelihood algorithms compute the direction and energy of the primary neutrino. Due to large directional uncertainties and statistical limits no definite astrophysical counterparts were found yet.

According to Gandhi et al. (1996) extraterrestrial neutrinos are expected to be produced via the decay of pions. These pions can be created by interacting protons at ultra-high energies. A promising astrophysical candidate class for the production of neutrinos are active galactic nuclei (Mannheim, 1993). Active galactic nuclei (AGN) belong to the most powerful radiation sources in the universe. This thesis studies the correlation of IceCube neutrinos with blazars, a subclass of AGN. Sources of Fermi's 3rd Catalog (Gasparrini et al., 2015) were subdivided in BL Lac like objects (BL Lac), flat-spectrum radio quasars (FSRQ) and blazar candidates of uncertain type (BCU). These three subcatalogs are tested for correlation with IceCube neutrinos.

To do so a maximum likelihood method based on the work of Glüsenkamp (2016) was used. The algorithm uses directional as well as energy information to test the correlation of a given catalog with IceCube neutrino events. In order to obtain correlation

propabilites, results of tested catalogs are compared to results of randomized catalogs. It is possible to check the sensitivity of the test method with a reference catalog. This reference catalog has to consist of random sources and inserted known neutrino positions. Results of this test can reveal, if the test method is sensitive enough to find correlations.

2 Neutrinos

Information for this chapter is taken from Bleck-Neuhaus (2013) and Povh et al. (2015).

2.1 Neutrino characterisation

Neutrinos are electrically neutral leptons with a spin of $\frac{1}{2}$, which behave fermionic. Leptons can be arranged in three families $\begin{pmatrix}\nu_\mathrm{e}\\ e^-\end{pmatrix}$, $\begin{pmatrix}\nu_\mu\\ \mu^-\end{pmatrix}$ and $\begin{pmatrix}\nu_\tau\\ \tau^-\end{pmatrix}$. In the standard model of particle physics (SM) every lepton has an associated antimatter antiparticle with the same mass and opposite charge: $\bar{\nu}_\mathrm{e}$, $\bar{\nu}_\tau$ and $\bar{\nu}_\mu$. Some theories beyond the standard model require the antiparticle to be identical with the particle itself, which then is called "majorana particle". This is hypothetical possible for electrically neutral particles, even though there are no majorana particles in the standard model yet. Whether the neutrino is a majorana particle or not is still a topic of current research.

In the SM neutrinos are assumed to be massless, even though experiments of the last years have shown that neutrinos indeed have a mass (see section 2.3). However the mass is very small, so far experiments could only give upper limits for the neutrino mass: $m_{\nu_\mathrm{e}} < 2\,\mathrm{eV}$, $m_{\nu_\mu} < 190\,\mathrm{keV}$ and $m_{\nu_\tau} < 18.2\,\mathrm{MeV}$. Last, gravitational effects are, as usual in particle physics, negligible small.

2.2 Neutrino interactions

There are two different kinds of weak interaction, the neutral current interaction (NC) and charged current interaction (CC). The mediator of the NC is the Z^0 bosons, whereas $W^{(+)}_{(-)}$ bosons are the mediators of CC interactions.

At high energies the dominating process, which is important for the high energy neutrino detection is the deep inelastic scattering (DIS). The two different interaction types are characterised by:

$$\mathrm{CC}: \qquad \nu_\ell + N \to \ell + X \tag{2.2.1}$$

$$\mathrm{NC}: \qquad \nu_\ell + N \to \nu_{\ell'} + X. \tag{2.2.2}$$

The incoming neutrino of flavor $\ell = e, \mu, \tau$ interacts with the nucleus N of an atom. In CC interactions the charged lepton is of the same generation as the primary neutrino

which is produced. In NC interactions the neutrino interacts with the nucleus, producing a neutrino of a different flavor. In both cases the remnant nucleus will cause a hadronic particle cascade.

The cross-section of neutrino-nuclei-interaction strongly depends on the parton density function of the nucleus. According to Gandhi et al. (1996) the cross-sections for CC and NC high energy interactions with a nucleus of mass M have the generell form of

$$\frac{d^2\sigma}{dxdy} \propto \frac{G_\mathrm{f}^2 M}{\pi} \left(\frac{M_\mathrm{W/Z}^2}{Q^2 + M_\mathrm{W/Z}^2} \right)^2 E_\nu, \tag{2.2.3}$$

where $G_\mathrm{f} = 1.16632 \times 10^{-5}\,\mathrm{GeV}^{-2}$ is the fermiconstant and $-Q^2$ is the relativistic squared momentum transfer from the incident neutrino to the outgoing lepton. Depending on the type of interaction (NC or CC) $M_\mathrm{W/Z}$ represents the mass of the intermediate bosons (Z^0 or $W^{\left(+\atop-\right)}$) with $M_\mathrm{W} = 80.385\,\mathrm{GeVc}^{-2}$ and $M_\mathrm{Z} = 91.1876\,\mathrm{GeVc}^{-2}$. For $Q^2 < M_\mathrm{W/Z}^2$ the intermediate boson mass dominates, which results in a linear increase of the cross-section, whereas higher values of Q^2 result in a lower increase of the cross-sections.

Even in the high energy regime the neutrino interaction of electrons is in generell negligible because of the small electron mass. The so called "Glashow" resonance of the W^- boson in $\bar{\nu}_e e$ interactions peaks at around 6.3 PeV. Here the resonant cross-section $\bar{\nu}_e e$ is larger than the νN cross-sections and therefore has to be included.

Figure 2.1 shows ultra-high energy (UHE) neutrino cross-sections for CC and NC interactions with electrons or nuclei. The Glashow resonance in the $\bar{\nu}_e e$ cross-section is clearly visible. Furthermore, it is clear that the order of magnitude of these neutrino cross-sections is very small compared to other particles. This results in very long mean free path lengths, which means neutrinos can travel extremely far before interacting with matter.

2.3 Neutrino flavor and neutrino oscillation

There are three neutrino flavor states $|\nu_\mathrm{e}\rangle$, $|\nu_\mu\rangle$ and $|\nu_\tau\rangle$ as well as three mass states $|\nu_1\rangle$, $|\nu_2\rangle$ and $|\nu_3\rangle$. The flavor states consist of a linear combination of mass states by the Pontecorvo–Maki–Nakagawa–Sakata matrix (PMNS matrix) U:

$$\begin{pmatrix} |\nu_\mathrm{e}\rangle \\ |\nu_\mu\rangle \\ |\nu_\tau\rangle \end{pmatrix} = \begin{pmatrix} U_\mathrm{e1} & U_\mathrm{e2} & U_\mathrm{e3} \\ U_{\mu 1} & U_{\mu 2} & U_{\mu 3} \\ U_{\tau 1} & U_{\tau 2} & U_{\tau 3} \end{pmatrix} \begin{pmatrix} |\nu_1\rangle \\ |\nu_2\rangle \\ |\nu_3\rangle \end{pmatrix}. \tag{2.3.1}$$

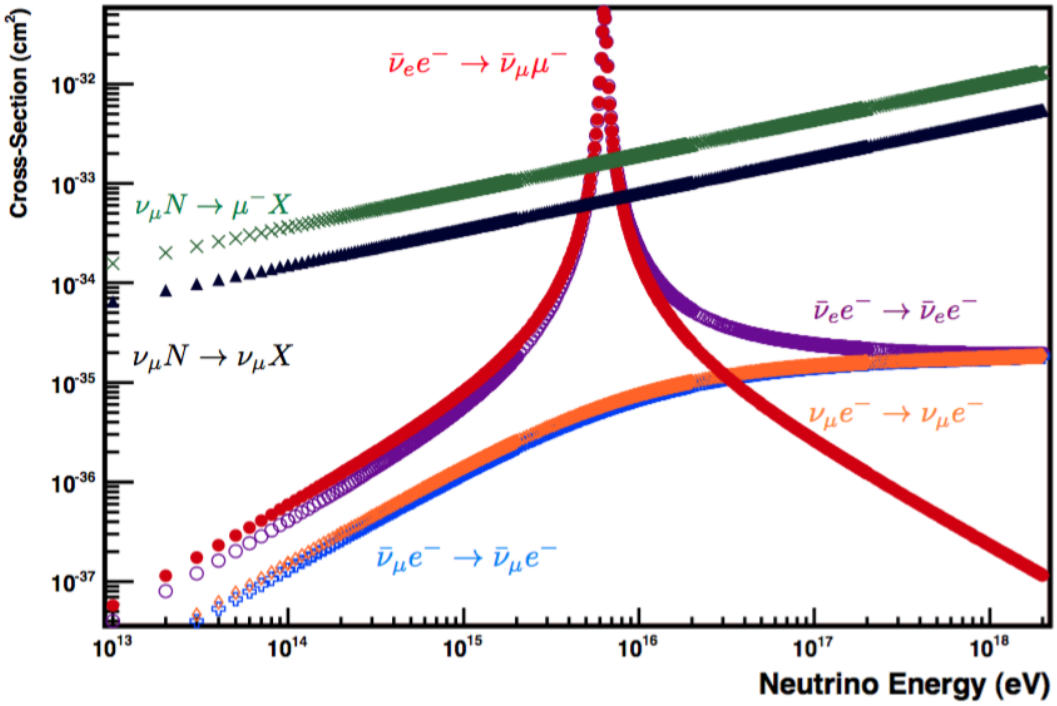

Figure 2.1: Neutrino cross-sections in the ultra-high energy regime for CC and NC interactions with electrons or nuclei. Credit: Formaggio and Zeller (2012)

In order to compute oscillation propabilites between two neutrino generations the equation can be reduced to

$$\begin{pmatrix} |\nu_e\rangle \\ |\nu_\mu\rangle \end{pmatrix} = \begin{pmatrix} \cos\theta & \sin\theta \\ -\sin\theta & \cos\theta \end{pmatrix} \begin{pmatrix} |\nu_1\rangle \\ |\nu_2\rangle \end{pmatrix}. \tag{2.3.2}$$

Now the propability to find a neutrino of the initial state $|\nu_e\rangle$ after the time t in the state $|\nu_\mu\rangle$ is given by

$$P_{\nu_e \to \nu_\mu} = 1 - \sin^2 2\theta \sin^2 \left(\frac{1}{4} \frac{(m_{\nu 2}^2 - m_{\nu 1}^2) c^3}{\hbar} \frac{t}{p} \right), \tag{2.3.3}$$

with $m_{\nu i}$ as mass of the state ν_i, Θ the mixing angle, c the speed of light in vacuum, $\hbar$ the reduced Planck constant and p the neutrino momentum. The electron neutrino has an oscillation propability between its initial flavor and the muon flavor, dependent on the difference of the state masses and time. As equation 2.3.3 shows neutrino oscillation is only feasible for neutrinos which have a mass. More precisely, neutrinos of different flavors must have a non-zero mass difference.

3 Neutrino detection

3.1 Cherenkov radiation

The following information are taken from Rädel and Wiebusch (2012) if not marked differently. If a charged particle propagates in a dielectric medium with refraction index n, it interacts with the medium via electromagnetic force and polarizes the electrons of the surrounding atoms. When the electrons move back they emit electromagnetic radiation. If the speed v of the charged particle exceeds the speed of light in this medium $c_{\text{medium}} = \frac{c_{\text{vacuum}}}{n}$ the emitted light forms a cone, analogous to the acoustic Mach cone. The cone has a half aperture θ which is given by

$$\cos\theta = \frac{1}{n\beta}, \tag{3.1.1}$$

where $\beta = \frac{v}{c}$. This light emission is called Cherenkov radiation. The number of photons N_γ, which are emitted per track length dx and energy intervall dE is given by the Frank-Tamm formula:

$$\frac{d^2N}{dxdE} = \frac{\alpha z^2}{\hbar c}\left(1 - \frac{1}{\beta^2 n^2}\right), \tag{3.1.2}$$

with finestructure constant α and Dirac constant $\hbar$ (Middell, 2008).

Relativistic particles emit typically around 250 photons per cm in ice ($n \approx 1.33$) with a wavelength between 300 nm and 500 nm. These wavelengths correspond to optical light in the blue to violett region. The light gets emitted under an angle of $\theta \approx 41\,\text{deg}$. If the medium is optically transparent the light can finally be detected by photomultipliers. The kinetic energy threshold for Cherenkov radiation is given by

$$E_{\text{ciritical}} \geq m\left(\frac{1}{\sqrt{1 - \frac{1}{n^2}}} - 1\right). \tag{3.1.3}$$

This corresponds to $E_{\text{critical},\mu} \approx 55\,\text{MeV}$ for muons and $E_{\text{critical,e}} \approx 0.26\,\text{MeV}$ for electrons in ice.

3.2 The IceCube detector

3.2.1 Structure

The IceCube neutrino detector is located close to the South Pole at the Amundsen-Scott South Pole station. The purpose of the detector is the indirect detection of neutrinos via Cherenkov radiation. The massive glacial ice acts both as the neutrino target as well as a transparent medium necessary for the detection of Cherenkov light. Figure 3.1 shows a schematic view of the IceCube detector. The detector consists of an array of 86 strings down to a depth of 2.45 km. Every string is instrumented with 60 Digital Optical Modules (DOMs) with a spacing of 17 m. The photomultiplier (PMTs) of the DOMs are responsible for the detection of Cherenkov photons. Their task is measuring the amplitude and the width of the incoming signal, as well as giving the signal an exact time stemp, which is crutial for event reconstruction. The digitized signals are then passed to the computers at the surface. Before the final storage filters are applied to reduce the size to forward the data via tapes or satellite transmission. Finally the data can be used for event reconstruction. According to The IceCube Collaboration (2008) and Abbasi, Abdou, and Abu-Zayyad (2010) each DOM contains a flasher board hosting 12 LEDs which can emit light pulses in the optical blue to UV regime detectable by other DOMs. The light flashes are used for physics simulations, calibrations and investigations of optical ice properties. The roughly 1.5 km ice on top of the DOM's shields the detector from cosmic rays. The complete volume of the detector corresponds to $1\,\mathrm{km}^3$.

The detector consists of different parts. The AMANDA detector was the precursor project to IceCube. To increase sensitivity for low energy neutrinos with $E_\nu \geq 10\,\mathrm{GeV}$ DeepCore has been built. According to Abbasi, Abdou, Abu-Zayyad, et al. (2012) it consists of eight strings with a smaller DOM spacing and uses photomultipliers (PMTs) with a higher quantum efficiency. DeepCore is furthermore located in a depth of around 2.1 km where the ice is more clear. On the surface the IceCube detector gets completed by the IceTop detector. IceTop is an array of 162 Cherenkov tanks, filled with ice and spread over 81 stations on top of the IceCube strings (Abbasi, Abdou, Ackermann, et al., 2013). Figure 3.2 shows a top view of the IceCube site with marked IceCube string and IceTop tank positions. IceTop allows to increase the sensitivity of IceCube for neutrino events with small Zenith angles through an effective background rejection.

3.3 Event reconstruction and signatures

Typical signatures in the IceCube detector are shown in Figure 3.3. Depending on the type of neutrino interaction there are plenty of different dedicated reconstruction algorithms. A small choice is introduced in the next sections. For more details refer to Aartsen, Abbasi, et al. (2014) and Ahrens et al. (2004).

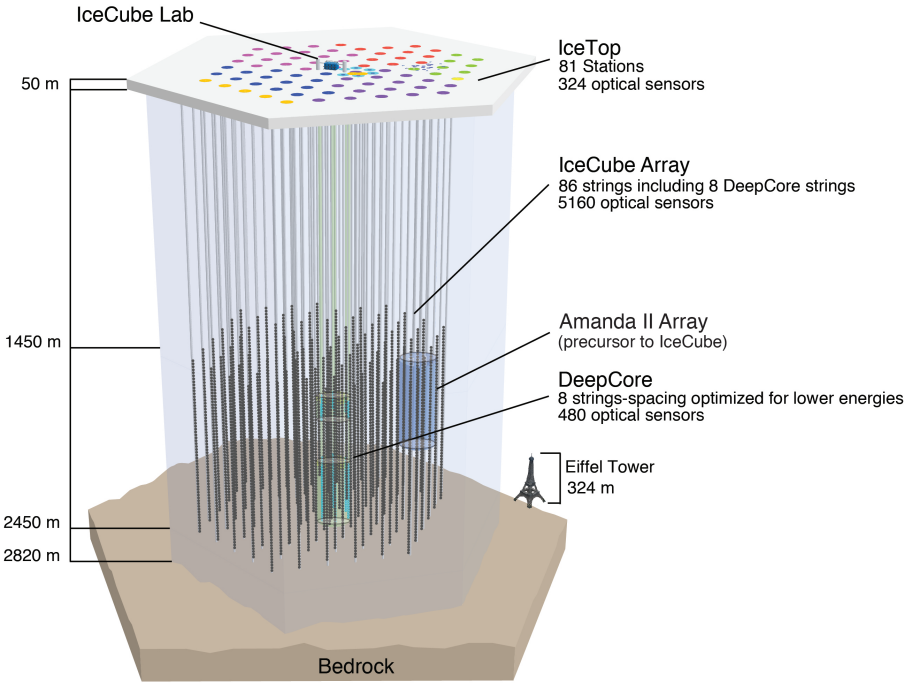

Figure 3.1: Schematic view of the IceCube detector. The Digital Optical Modules on the 86 strings of IceCube detect Cherenkov radiation and transmit the signal to the IceCube Lab on the surface. Credit: IceCube-Gen2 Collaboration et al. (2014).

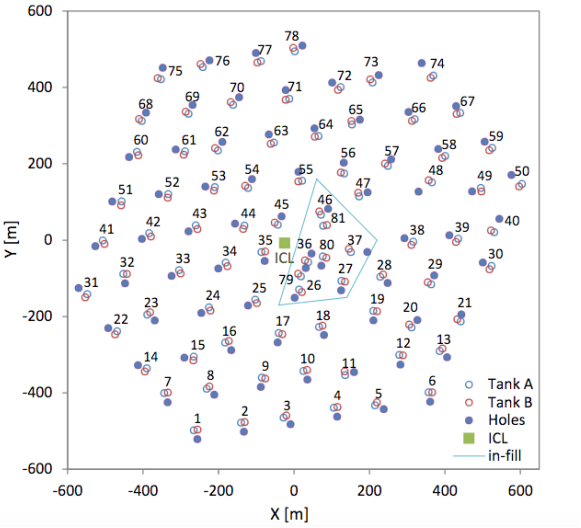

Figure 3.2: Top view of the IceCube site. The positions of the IceCube strings and the IceTop Cherenkov tanks A and B accumulated around the IceCube Lab (ICL). Credit: Abbasi, Abdou, Ackermann, et al. (2013).

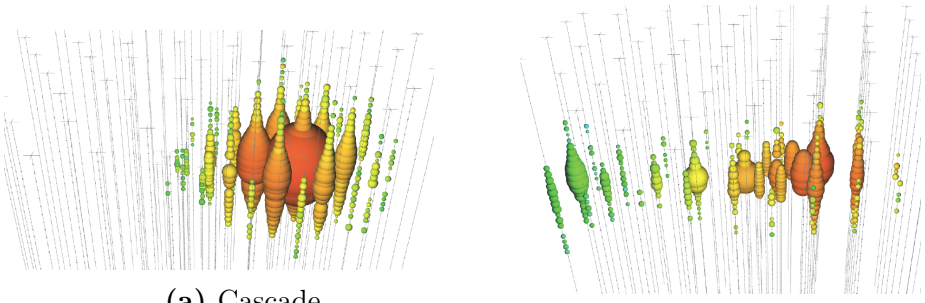

(a) Cascade

(b) Track

Figure 3.3: Simulated signatures in the IceCube detector. The grey lines represent the strings, the spheres represent the DOMs, their size is proportional to the received light amplitude and the colors show time evolution (from red to green). Electron induced cascades appear as point-like sources, whereas muons leave tracks which indicate the propagation path. Credit: IceCube Collaboration (2016).

3.3.1 Energy reconstruction

When the neutrino interacts with ice it creates an hadronic shower at the interaction vertex. Furthermore, the emerging lepton will lose its energy, depending on the type of neutrino and trigger additional showers. The number of Cherenkov photons emitted by resulting secondary particles and electromagnetic (EM) showers is proportional to the integrated path length of the charged particles and the total energy of these particles. This is why the total light yield can be used for reconstruction of the primary neutrino energy. There are basically two different types of IceCube events: tracks and cascades.

For energy reconstruction the energy deposition E can be approximated by comparing the number of photons of a PMT k to the light-yield scaling function Λ of a template event. These template events are tabulated data, generated by Monte Carlo simulations of light propagation in ice. These simulations take the detector response into account, as well as ice properties in different layers. The likelihood for a shower of deposited energy E, detected by a number of photons in a PMT k is Poisson distributed and hence has the form:

$$\mathcal{L} = \frac{\lambda^k}{k!} \cdot e^{-\lambda}, \tag{3.3.1}$$

where $\lambda = \Lambda E$ is the mean of the distribution. Adding up all PMTs, applying a ln function and maximizing it leads to:

$$E = \frac{\sum_{PMTs} k_j}{\sum_{PMTs} \Lambda_j}. \tag{3.3.2}$$

Additional photon contributions ρ, e.g. PMT noise, can be introduced by changing the mean value to $\lambda = \Lambda E + \rho$, which leads to the equation

$$\sum_{PMTs} \Lambda_j = \sum_{PMTs} \frac{k_j \Lambda_j}{E\Lambda_j + \rho_j}. \tag{3.3.3}$$

Here solutions can be found only with numerical algorithms. Furthermore, it is possible to use the time information of the PMTs with the formulas 3.3.2 and 3.3.3 by categorizing the arrived photons in time bins and interpreting k and Λ as light per bin time instead of light per PMT. However, including time information only leads to a big increase of energy reconstruction performance for multiple emitting sources, but not for single sources.

The performance of energy reconstruction depends strongly on the light-yield scaling function Λ. There are many candidate functions, but generally they discriminate only between tracks or cascades. An analytic approximation of the expected light yield under the assumptions of little scattering, straight photon propagation and an exponential

photon density decrease leads to:

$$\mu(r) = n_0 A \cdot \frac{1}{4\pi} e^{-r/\lambda_\mathrm{p}} \frac{1}{\lambda_\mathrm{c} r \tanh(r/\lambda_\mathrm{c})}, \tag{3.3.4}$$

where $\lambda_\mathrm{c} = \frac{\lambda_\mathrm{e}}{3\eta}$, $\eta = e^{-\lambda_\mathrm{e}/\lambda_\mathrm{a}}$ for point sources, and

$$\mu(r) = l_0 A \cdot \frac{1}{2\pi \sin(\theta_\mathrm{c}) e^{-r/\lambda_\mathrm{p}}} \frac{1}{\sqrt{\lambda_\mu r} \tanh \sqrt{r/\lambda_\mu}}, \tag{3.3.5}$$

where $\sqrt{\lambda_\mu} = \frac{\lambda_\mathrm{c}}{\sin\theta_\mathrm{c}} \sqrt{\frac{2}{\pi\lambda_\mathrm{p}}}$ for tracks, and $\lambda_p = \sqrt{\lambda_a \lambda_e/3}$.

n_0 is the number of photons, emitted by a point source, l_0 is the number of photons per meter from a uniform track source, A is the effective photon collection area of the PMT and θ_c the Cherenkov angle. λ_a is the absorption length and λ_e denotes the effective scattering length. The parameter r represents the distance of closest approach to the source.

For the reconstruction of event energies a linear response of the detector in energy and time is important. This fact shows the need for dedicated calibration methods to guarantee the linearity. The DOMs offer integrated LEDs, as well as in-ice lasers, for calibration purposes. With these tools and ice taken from the boreholes during construction it is possible to model the propagation properties of photons in ice. Furthermore, it is possible to use minimum-ionizing muons which have a well known constant light emission as standard brightness candles to probe the detector in the low energy regime. The 337 nm pulsed nitrogen lasers produce an output corresponding approximately to the light output of $1 - 100\,\mathrm{PeV}$ EM showers. This allows the study of linearity in the high energy regime, where minimum-ionizing muon methods fail.

Cascades: On the scale of the IceCube instrumented volume the light deposition is independent from energy. Using cascade templates makes the reconstruction of the energy with the method explained before possible. The maximisation of the likelihood is done numerically and the maximum is calculated with the so-called "Non-monotonic Maximum Likelihood" algorithm (NMML).

For NC interactions the reconstructed deposited energy is only a lower limit of the neutrino energy. Here the outgoing neutrino carries an unknown amount of energy out of the detector. For ν_e CC interactions on the other hand, the deposited energy is nearly identical to the energy of the neutrino. IceCube is not able to distinguish between different cascade event types. This is the reason why all reconstructed cascade energies are only a lower limit of the neutrino energies.

Tracks: The energy reconstruction of tracks is more complicated than the reconstruction of cascade events. At energies $E \lesssim 100\,\mathrm{GeV}$ the muon range in ice is smaller than

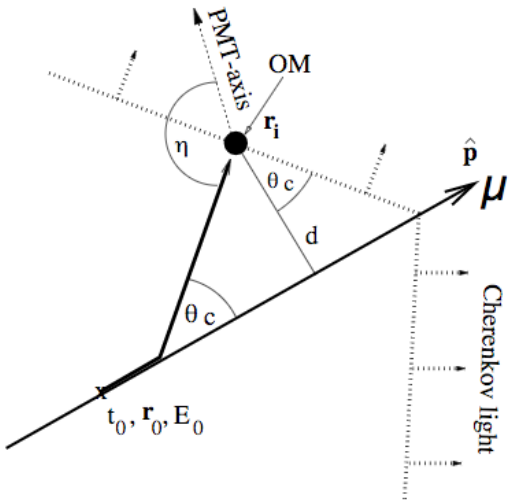

Figure 3.4: Outline of μ-track reconstruction parameters. Credit: Ahrens et al. (2004)

the length of the IceCube detector. But for energies higher than this limit the muon range exceeds the detector length. So either the muon's point of origin or the last part of the muon track lie outside the detector. This is the reason why the reconstructed energy only provides a lower limit. Therefore, the energy must be estimated only by properties of the emitted light like the differential energy loss rate $\frac{dE}{dx}$. Due to energy losses dominated by stochastic processes as bremsstrahlung, pair production and photonuclear interactions fluctuations of the amount of energy distributed in the detector are very large.

3.3.2 Directional reconstruction

Similar to the energy reconstruction, there are plenty of methods for the directional reconstruction of IceCube events. Basically it is possible to group these methods in track and shower reconstruction algorithms.

Tracks: Assuming the Cherenkov radiation of a μ-track is generated cone-like by an infinite track with $\beta = 1$ the track can be described by the following set of parameters:

$$\vec{a} = (\vec{r}_0, t_0, \hat{p}, E_0). \tag{3.3.6}$$

An explanatory outline is shown in Figure 3.4 .

According to Ahrens et al. (2004) these paramters can be obtained by maximizing the likelihood

$$\mathcal{L}(\vec{x}|\vec{a}) = \prod_i p(x_i|\vec{a}), \tag{3.3.7}$$

which consists of the propability distribution functions $p(x_i|\vec{a})$ for observing the measured value x_i for given parameter values $\vec{a}$. For track reconstruction the most important set of measured data is the timing information of photon hits in the PMTs. Here the propability distribution function (PDF) for the k^{th} out of N photons is given by

$$p_N^k(t_{res}) = N \cdot \binom{N-1}{k-1} \cdot p_1(t_{res}) \cdot (1 - P_1(t_{res}))^{N-k} \cdot P_1(t_{res})^{k-1}, \tag{3.3.8}$$

where P_1 denotes the cumulative single photon distribution. The factor p_1 considers the photon propagation through ice and is obtained by simulations. The time residual $t_{res} \equiv t_{hit} - t_{geo}$ is defined as the difference of the observed photon hit time and the hit time expected for a direct photon.

Cascades: The Likelihood algorithms for cascade reconstruction are very similar to the ones of the muon track reconstruction. According to Kowalski (2004) an often used PDF parametrization for the interaction vertex Likelihood at a distance d is the so called Pandel function:

$$p(d, t_{res}) = \frac{\tau^{-d/\lambda} t^{d/(\lambda-1)} e^{-(t/\tau + c_{\text{ice}} t/X_0 + d/X_0)}}{\Gamma(d/\lambda)}. \tag{3.3.9}$$

The parameter X_0 is the absorption length, λ/t the scattering length/time, c_{ice} the speed of light in ice and Γ the Gamma function. Below 10 PeV cascades have characteristic lengths of several meters (*Improved Reconstruction of Cascade-like Events in IceCube* (2009)). As the spacing of the DOMs is larger, cascades appear as point-like sources. However, the angular emission profile is anisotropic, since the photons are preferably emitted in direction of the Cherenkov angle. As the dust layers in the glacial ice have a big influence on the light propagation, numerical photon propagation simulations have to be taken into account. Thus, for the reconstruction of the direction the angular average number of photons can be compared to Monte-Carlo simulations.

3.3.3 Effective area and detector sensitivity

The effective area A_{eff} is a measure of a detectors sensitivity and performance. The effective area is dependent on the Zenith angle and the energy of the incoming neutrino. According to Voigt (2008) it is possible to calculate the number of measured events

$$N = t \cdot \int A_{\text{eff}}(E, \theta) \phi(E, \theta) dE d\Omega, \tag{3.3.10}$$

in a given time t of a certain flux $\phi(E, \theta)$. Figure 3.5 shows the energy and zenith angle dependent effective areas for all three neutrino generations. The effective areas for electron neutrinos show the characteristic peak of the Glashow resonance in the energy range of $6 - 7$ PeV. The earth can shield the IceCube detector against background par-

ticles, while neutrinos still can be able permeate the earth. However, at high energies at Zenith angles $\theta \geq 90\,\mathrm{deg}$ the higher neutrino cross sections extinguish neutrino contribution from below the horizon. The effective areas of IceCube for these directions become smaller, which means that the earth is more opaque to these neutrinos. In order to increase IceCubes sensitivity for the southern sky IceTop was build. Here, cosmic ray induced muons dominate the neutrino spectrum. With IceTop it is possible to detect coincident particles of cosmic rays and therefore reject background in the detector effectively. For more information see Auffenberg (2013).

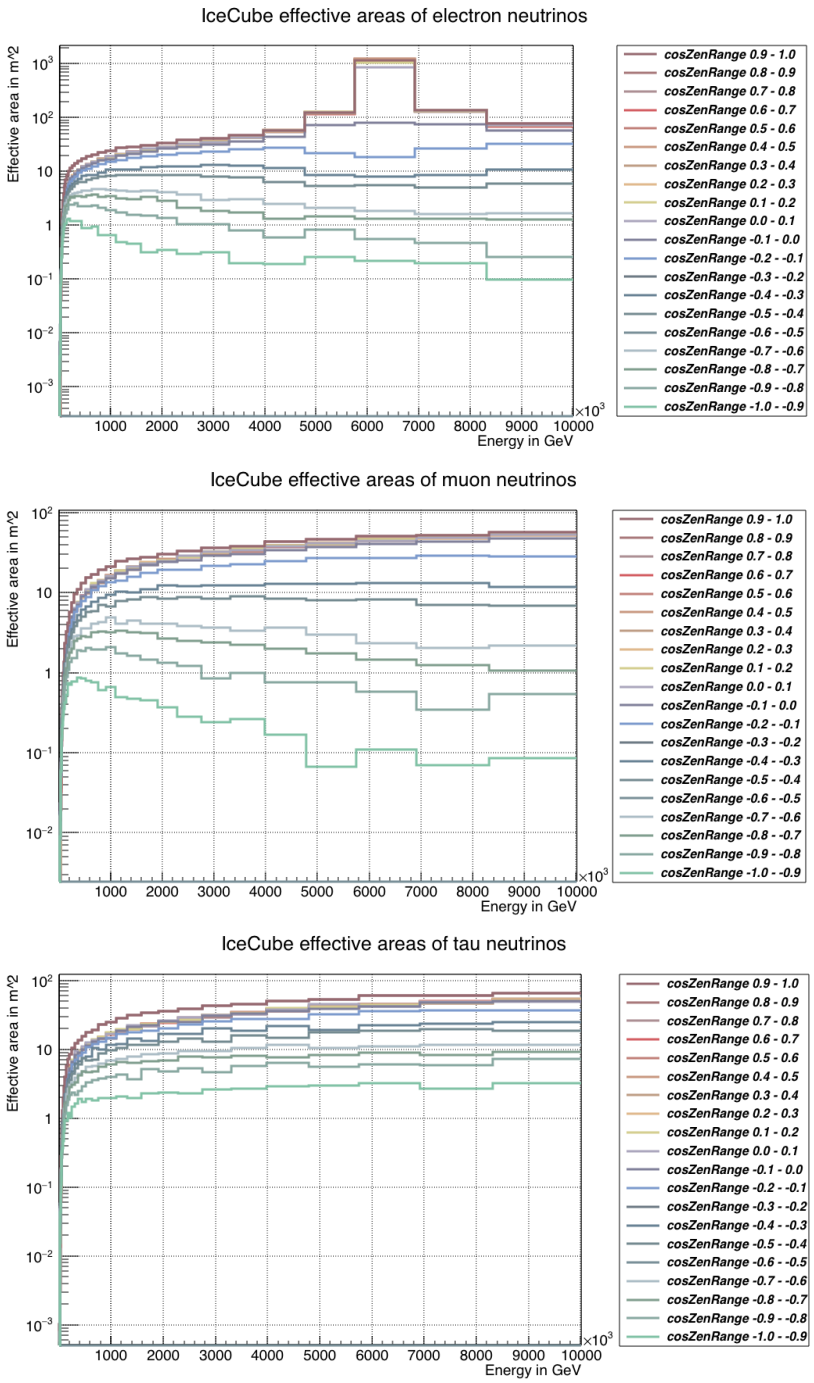

Figure 3.5: IceCubes effective areas as a function of the neutrino energy. Current effective areas are given as zenith angle dependent data. At high energies the earth becomes opaque to neutrinos. In the effective areas for electron neutrinos the Glashow resonance is visible.

4 Active galactic nuclei

4.1 Neutrino production mechanisms

There are many possible astrophysical objects which could produce neutrinos. The mechanisms for the production of neutrinos are basically the same for all sources. According to Gandhi et al. (1996) neutrinos in the ultrahigh-energy regime (UHE: $E \gtrsim 10^{12}\,\mathrm{eV}$) are produced by the decay of $\pi^{(+)}_{(-)}$ mesons and those further decay of μ particles:

$$\begin{aligned} \pi^+ &\to \nu_\mu + \mu^+ \\ \hookrightarrow \mu^+ &\to \bar{\nu}_\mu + \nu_e + e^+ \\ \pi^- &\to \bar{\nu}_\mu + \mu^- \\ \hookrightarrow \mu^- &\to \nu_\mu + \bar{\nu}_e + e^- \\ \pi^0 &\to \gamma + \gamma \end{aligned} \tag{4.1.1}$$

In astrophysical sources the required π particles can be created by the interaction of hadrons

$$\begin{aligned} p + p &\to \pi^0 + p + p \\ p + p &\to \pi^+ + p + n \end{aligned} \tag{4.1.2}$$

and photohadronic interactions

$$\begin{aligned} p + \gamma &\to \Delta^+ \to \pi^+ + n \\ p + \gamma &\to \Delta^+ \to \pi^0 + p. \end{aligned} \tag{4.1.3}$$

Assuming an equal production of π^+ and π^0 would result in a neutrino-photon ratio of

$$\gamma : \nu_\mu : \nu_e : \nu_\tau = 2 : 2 : 1 : 0. \tag{4.1.4}$$

Taking the effect of neutrino oscillation over comsic distances into account, one can expect an equal mixing of neutrino flavours

$$\gamma : \nu_\mu : \nu_e : \nu_\tau = 2 : 1 : 1 : 1. \tag{4.1.5}$$

This leads to an approximate limit on the flux of neutrinos and γ-photons: $F_\nu \sim F_{\mathrm{gamma}}$.

Blazars are a subclass of active galactic nuclei (AGN) with a bolometric output some-

times exceeding $L > 10^{48} \frac{\text{erg}}{\text{s}}$ (Tavecchio, 2010). Since this class of extragalactic astrophysical objects dominates the sky at energies above 100 MeV (Tavecchio, 2010), blazars are promising candidates for UHE neutrino sources.

4.2 Active galactic nuclei

Active galactic nuclei (AGN) belong to the most powerful sources in the universe. With very high luminosities concentrated in a compact region they are a stage for rare and extreme physics. The information for this chapter is taken from Krawczynski and Treister (2013) and Beckmann and Shrader (2012).

4.2.1 Structure

A schematic structure of AGN is shown in Figure 4.1. It is believed that the center of AGN is a supermassive black hole (SMBH) with a mass up to $M_{\text{SMBH}} = 10^{10}\,\text{M}_\odot$. A disk of dust, gas and ionized particles is surrounding the SMBH. The SMBH is accreting material of this so called accretion disk with the rate

$$\dot{M} = \pi \rho v r^2, \tag{4.2.1}$$

where r is the distance to the SMBH, ρ is the density and v is the velocity. In this process angular momentum gets transfered from the inside of the accretion disk to the outside, while gravitational energy is released as radiation with the luminosity:

$$L = \frac{G M_{\text{SMBH}}}{R} \cdot \dot{M}, \tag{4.2.2}$$

where G denotes the gravitational constant and R the distance from a mass element M to the center. The accretion caused by the pressure gradient of the in-falling matter

$$\frac{dP}{dr} = \frac{-G M_{\text{SMBH}} \rho}{r^2} \tag{4.2.3}$$

is limited due to the radiation pressure

$$\frac{dP}{dr} = \frac{-\sigma_{\text{T}} \rho}{m_{\text{p}} c} \frac{L}{4\pi r^2} \tag{4.2.4}$$

defining the Eddington luminosity

$$L_{\text{Edd}} = \frac{4\pi G M_{\text{SMBH}} m_{\text{p}} c}{\sigma_{\text{T}}}. \tag{4.2.5}$$

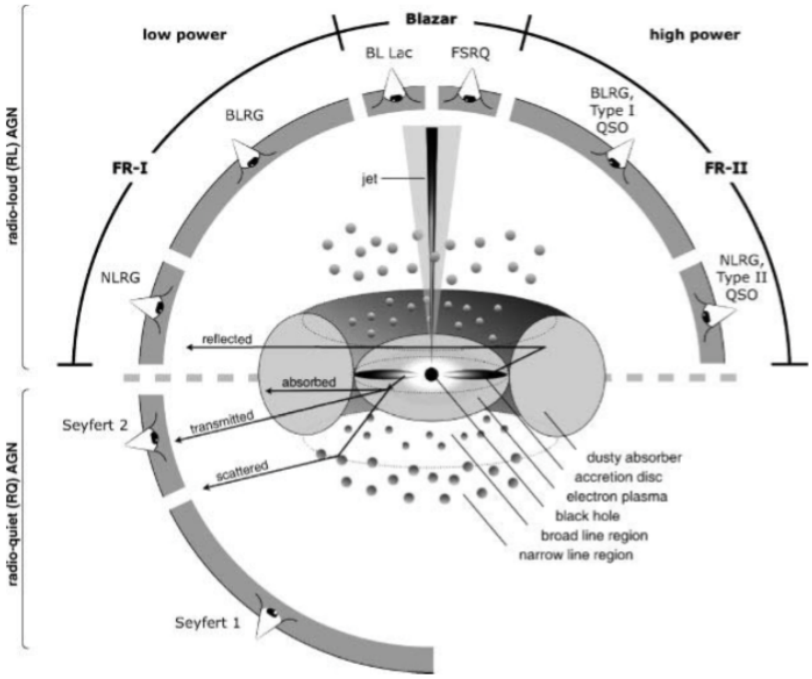

Figure 4.1: Schematic structure of AGN and the unification scheme. The upper part shows a radio-loud AGN, which features a relativistic jet. The lower part shows a radio-quiet AGN, where no jet is present. The unification model assumes that all observed AGN classes can be explained by different viewing angles and radio-loudness. Credit: Beckmann and Shrader (2012)

Here m_p is the proton mass, σ_T is the Thomson cross-section and c the vacuum velocity of light. In $15-20\%$ of all AGN, this accretion engine, together with effects like viscious dissipation (Shakura and Sunyaev, 1973), is able to power a relativistic jet. These AGN are called "radio-loud", whereas AGN which do not show a jet are called "radio-quiet". The distinction is given by the ratio of the radio flux at 5 GHz to the flux in the optical range:

$$R^* \equiv \frac{f_{5\,\mathrm{GHz}}}{f_\mathrm{optical}}. \tag{4.2.6}$$

Depending on the exact definition radio-quiet objects often show $0.1 < R^* < 1$, whereas radio-loud obejcts have larger R^* values. The jet is assumed to consist of strong spiral-formed magnetic fields. Inside the jet highly collimated, relativistic plasma structures are launched from the SMBH along the direction of the rotation axis of the central SMBH. These jets can reach extents in kilo- and even megaparsec scales into space. Jet emission processes are regarded detailed in section 4.2.4

The broad line region (BLR) is a spheroidal shaped region around the accretion disk. The BLR consists of dust and gas clouds. Due to the energetic emission of the cen-

tral engine the BLR side facing the SMBH is higly ionized. The ionizing emission gets absorbed, which leads to a neutral or less ionized opposite side. This manifests in oberservation of high-ionization lines from the front and low-ionization lines from the back. The BLR emission lines show a strong broadening, the so-called Doppler broadening, which is characteristic for high velocities. The narrow line region (NLR) lying further outside which sheats the BLR shows characteristic emission lines, too. But the NLR emission lines are not as broad as the BLR emission lines, which indicates slower velocities. Further information can be taken from Gaskell (2009). A big torus consisting of dust is lying outside next to the accretion disk. The absorbing characteristics of this dust torus are very important for observational properties of AGN.

4.2.2 Classification

There are a variety of different AGN subclasses with different individual characterisitics at all wavelengths. Due to the historical development AGN classes were defined by observational properties. The distinction can be made by various properties, like the orientation of the source, the radio flux or optical emission lines. Spectral energy distributions (SEDs) show for each class typical features, and peak positions in these SEDs can also be used for classification.

Seyfert galaxies: Seyfert galaxies belong to the radio-quiet AGN, so they do not have a relativistic jet. In the optical regime they appear point-like with a bright core. Seyfert galaxies are characterised by ionized, narrow emission lines. They can be separated further, as some Seyfert galaxies show additionally broad Balmer lines in their spectra, caused by Doppler broadening. This type is called Seyfert 1, whereas Seyfert 2 only emits narrow lines, which are mostly less dominant than the surrounding galaxy.

Radio galaxies: Galaxies which show bright radio jets and huge radio luminosities are classified as radio galaxies. This class can be further subdivided into Faranoff-Riley galaxies of type I and II (FR I/II), based on the radio morphology. FR I is the low-luminosity subgroup which shows mainly emission of the region close to the center. The luminosity of the jets of FR I radio galaxies is decreasing with increasing distance to the AGN core. FR II on the other hand show high luminosities, dominated by the bright lobes of the radio jets.

Quasars: Quasi-stellar radio sources (Quasars) were discovered in late 1950s and early 1960s as radio sources. They have optical counterparts that show star-like emission. Quasars belong to the most luminous AGN. They have optical spectra very similar to Seyfert galaxies, only defined by higher absolute magnitudes of $M_{\mathrm{B}} > 23\,\mathrm{mag}$. There are both radio quiet and radio loud quasars, and they can usually be found at high redshifts z.

Blazars: Blazars are distinguished by a jet orientation, which points close to the line of sight to the observer. This results often in an extreme variability of flux. Time scales for variations range between a year down to intraday variability (IDV). The emission of blazars reaches throughout the electromagnetic spectrum from radio frequencies up to very high energies (VHE) of over 1 TeV. Blazars can be subdivided in BL Lacs and FSRQs (Flat Spectrum Radio Quasars). Blazars often show weak emission lines. A criterion for distinction is the equivalent width of the emission lines, where FSRQs show broad lines, whereas in BL Lacs often no emission lines are found. A further distinction can be made by the position of peaks in the SEDs. Sources, which are dominant at X-ray energies are therefore called high-frequency peaked BL Lacs (HBLs), whereas sources with a strong radio flux are declared as low-frequency peaked BL Lacs (LBLS). The fraction of time in which a blazar is variable (duty cycle) is strongly dependent on the source SED. While HBLs have duty cycles of $\lesssim 0.4$, LBLs have duty cycles of up to ~ 0.8 and show much stronger variability. Variability can occur at all energies, but Lovell et al. (2008) showed, that the radio IDV variability is not source intrinsic, but correlates with scintillation in the turbulent, ionized interstellar medium of our own Galaxy. For more information about variability see Wagner and Witzel (1995).

4.2.3 Unification:

The unificated model explains all diverse phenomena of the AGN zoo by one general model. Urry and Padovani (1995) introduced the idea that these different appearances in observation are due to different viewing angles, taking radio-loudness properties aside. Depending on the viewing angle, geometrical effects and absorption causes different effects for the observer. For example, in Seyfert II galaxies the emission of the broad line region is absorbed by the cold dust torus resulting in observation of narrow lines only. A schematic sketch is shown in Figure 4.1. The upper part shows the unification model for radio-loud AGN which feature a relativistic jet, whereas the lower part shows the unification for radio-quiet AGN. Since the absorption due to different viewing angles alone cannot explain all differences in AGN subclasses, there are additional factors discussed. Among these factors is the power of the central enginge, which is in radio-loud cases capable of producing the relativistic jets. Further factors can be the spin and the mass of the black hole in the center of the AGN.

4.2.4 Blazar emission processes

Figure 4.2 shows a SED of a blazar. Contributions of different physical processes in the AGN jet yields a characteristical double-hump structure. The first hump in the radio regime is caused by synchrotron radiation. Current theoretical models assume blobs of relativistic charged particles moving up in the jet with the velocity v close to the speed of light. They are accelerated due to first- and second-order fermi acceleration, which were proposed by Fermi (1954). In this process particles gain energy while bouncing

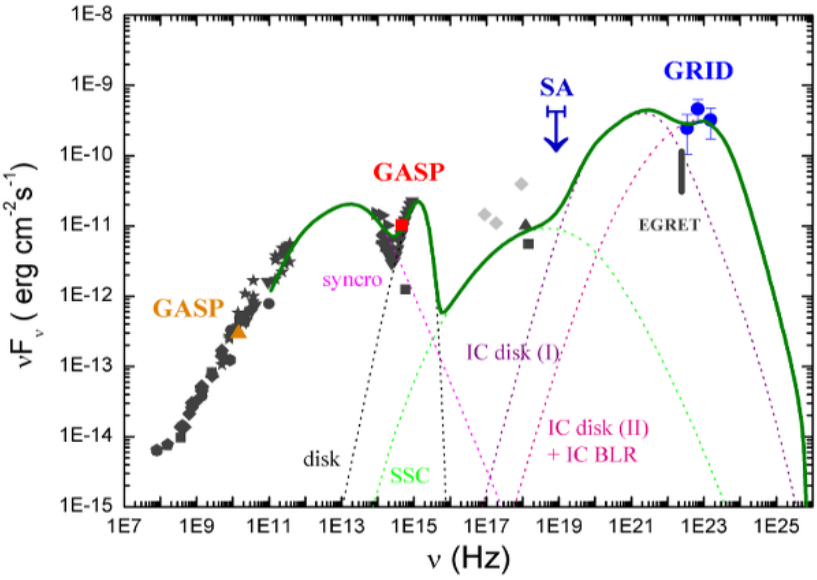

Figure 4.2: Spectral energy distribution (SED) of a blazar. Contributions of different physical processes like synchrotron radiation and inverse compton scattering yield a characteristic double-hump structure. The big blue bump causes a third sharp peak at the end of the low-energy hump. Credit: Pucella et al. (2008).

between dense shock regions in the jet. Due to strong magnetic fields B in the jet these charged particles with elementary charge e and mass m are subject to the Lorentz force and get accelerated by

$$\frac{d}{dt}(\gamma m\vec{v}) = \frac{e}{c}(\vec{E} + \vec{v} \times \vec{B}), \tag{4.2.7}$$

which results in a helical motion. According to Rybicki and Lightman (2004) a non-thermal synchrotron radiation is given by a power-law of the form: $n(\gamma)d\gamma = n_0\gamma^{-p}d\gamma$. Together with the spectral energy distribution of a single electron $P_\nu(\gamma)$ this results in an emitted power given by

$$P(\nu) = \int_1^{\text{inf}} P_\nu(\gamma)n(\gamma)d\gamma \propto \nu^{-\alpha}, \tag{4.2.8}$$

with an spectral index of $\alpha = \frac{p-1}{2}$. Thus, the spectrum will again be a power-law with index α.

In the UV regime there is a hump on-top of the low energy hump for some AGN, which is called the big blue bump. As suggested by Shields (1978) this emission arises due to thermal emission of the accretion disk. This radiation provides seed photons for the later explained $p\gamma$ interaction.

For the high energy emission of blazars which is represented by the second big hump,

different models are presented following Mannheim (1993) and Böttcher et al. (2013). The leptonic model assumes only electrons e^- (and positrons e^+) contributing to the emission. The high energy emission is produced by inverse Compton scattering. In this process ultrarelativistic electrons which already produced synchrotron photons, scatter low energy photons to high energies:

$$e^- + \gamma_{\mathrm{low-energy}} \rightarrow e^- + \gamma_{\mathrm{high-energy}}. \tag{4.2.9}$$

According to Longair (2011) the energy loss rate of the electron in its rest frame is given by

$$-\left(\frac{dE}{dt}\right) = \sigma_{\mathrm{T}} c u_{\mathrm{rad}}, \tag{4.2.10}$$

where σ_{T} is the Thomson cross-section and u is the energy density of radiation. High energy photons in this model would reach energies up to the $10 - 100\,\mathrm{TeV}$ range (Katz and Spiering, 2012).

Lepto-hadronic models on the other hand assume that electrons and protons are accelerated to ultrarelativistic energies. In this process protons exceed the threshold for the meson production shown in eq. 4.1.1. A schematic figure of a lepto-hadronic AGN jet model is shown in Figure 4.3. Here synchrotron photons provide seed photons for the pion production, which then decay into neutrinos and leptons. According to (Katz and Spiering, 2012) the energies in this model would overtop leptonic models with energies up to the PeV regime. Due to absorption of these UHE photons by the cosmic microwave background (CMB) in the process

$$\gamma_{\mathrm{PeV}} + \gamma_{\mathrm{CMB}} \rightarrow e^+ + e^- \tag{4.2.11}$$

the detection of these photons on earth is not possible. So far non of the models could get ruled out due to their common ability to fit measured SEDs, but detection of neutrino emission of AGN would be the key to confirm hadronic models.

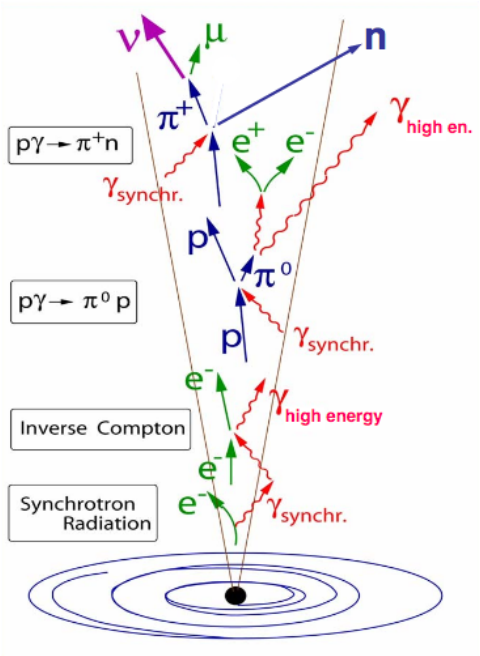

Figure 4.3: Schematic figure of a lepto-hadronic AGN jet model. Photons produced by synchrotron radiation are able to create together with protons π-particles. The decay of these pions creates among other particles neutrinos. Credit: Katz and Spiering (2012).

5 Analysis

The computational implementation of the basic algorithms was developed by Wiehl (2016). In this work the method was enhanced by taking energetic dependences into account and implementing new effective areas. The main focus of this work was the developement of test methods which result in statistical evidences.

5.1 Unbinned maximum likelihood method

The computational calculations of this work are based on the so-called maximum likelihood method as described in Blobel and Lohrmann (1998). This method calculates the parameters of a statistical model to achieve maximum agreement with a given sampling of data.

The propability density function (PDF) for an independent and identical distributed sample with a set of parameters θ is given by:

$$f(x_1, x_2, ..., x_n|\theta) = \prod_{i=1}^{n} f(x_i|\theta). \tag{5.1.1}$$

Considering the sampling x_i fixed and the parameters θ as free variables this function is called the likelihood:

$$\mathcal{L}(\theta; x_1, ..., x_n) = \prod_{i=1}^{n} f(x_i|\theta). \tag{5.1.2}$$

Obviously, the numerical calculation get facilitated by taking the logarithm of the likelihood:

$$\log(\mathcal{L}) = \sum_{i=1}^{n} \log(f(x_i|\theta)). \tag{5.1.3}$$

In order to obtain the set of parameters θ which produce the best fit of the statistical model to the observed data, it is necessary to maximise the likelihood function.

The algorithm of this work is based on a slightly different variation, an "*unbinned maximum likelihood*", proposed by Glüsenkamp (2016). Here, the likelihood has the following form:

$$\log(\mathcal{L}(n_s)) = \sum_{i=1}^{N} \log\left(\frac{n_s}{N} \cdot S_i + (1 - \frac{n_s}{N}) \cdot B_i\right). \tag{5.1.4}$$

S_i and B_i are the source and background propability distribution functions and N is the total number of neutrino events. In the end the likelihood function is maximized in respect to the parameter n_s, which represents the number of neutrinos, which most likely originate from sources of the tested catalog. $(N - n_s)$ on the other hand represents the number of neutrinos of the tested neutrino sample, which most likely do not fit to the tested source catalog, e.g. events produced by background particles in the detector.

5.1.1 Signal propability distribution function S_i

The signal propability distribution function (PDF) for the ith event is defined as:

$$S_i = \frac{\sum_{j=1}^{N_{\text{sources}}} S_j(\vec{x}_i, \sigma_{\vec{x}_i}) \cdot \omega_j \cdot \epsilon_j(E_i)}{\sum_{j=1}^{N_{\text{sources}}} \omega_j}. \tag{5.1.5}$$

S_j is the signal point spread function (PSF) which takes the angular distance from the source j to the neutrino event i into account. The signal PSF is modeled as a Gaussian

$$S_j = \frac{1}{\sqrt{2\pi \cdot \sigma_{\vec{x}_i}}} \cdot e^{-\frac{\theta(|\vec{x}_i - \vec{x}_j|)}{2 \cdot \sigma_{\vec{x}_i}}}, \tag{5.1.6}$$

where $\theta(|\vec{x}_i - \vec{x}_j|)$ is the angular distance between the celestial event position $\vec{x}_i$ and the celestial source position $\vec{x}_j$. The width of the Gaussian is given by the angular error $\sigma_{\vec{x}_i}$ of the event detected by IceCube. ω_j is a source dependent weighting factor. As the neutrino flux of blazars is assumed to be proportional to the gamma-ray flux (see section 4.1), following weighting scheme is used:

$$\omega_j = \frac{F_j}{F_{\text{max}}}. \tag{5.1.7}$$

F_j is the flux in the gamma-ray band of the relevant source j and F_{max} is the maximal gamma-ray flux of all sources of the tested catalog. Since the tested catalogs are not complete concerning gamma-ray fluxes, sources with missing flux values get the minimal flux value of all sources in order to avoid computing problems.

The last term in equation 5.1.5 is the energy PDF $\epsilon_j(E_i)$ which has the following form:

$$\epsilon_j = E_i \cdot E_{\text{PSF}}(E_i, E_j, \sigma_{E_i}) \cdot A_{\text{eff}}(E_i, \vec{x}_j). \tag{5.1.8}$$

Each signal event from a source corresponds to a Monte-Carlo simulated energy E_j. We assume that the Monte-Carlo simulated energy of the source should fit the reconstructed energy of the neutrino event E_i. This dependance gets modelled analogous to the signal PSF (eq. 5.1.6) by a 1D Gaussian depending on the energy difference $E_i - E_j$ and the

energy reconstruction error σ_{E_i}:

$$E_{\mathrm{PSF}} = \frac{1}{\sqrt{2\pi \cdot \sigma_{E_i}}} \cdot e^{-\frac{|E_i - E_j|}{2 \cdot \sigma_{E_i}}}, \tag{5.1.9}$$

$$\text{with} \begin{cases} \sigma_{E_i} = \sigma^{-}_{E_i} \text{ for } E_i - E_j < 0 \\ \sigma_{E_i} = \sigma^{+}_{E_i} \text{ for } E_i - E_j > 0 \end{cases}. \tag{5.1.10}$$

The width of the Gaussian is asymmetric because of an asymmetric energy reconstruction error. Both sides of the Gaussian are separately normalized. The exact energy spectrum is described in section 5.2. As the response of the detector is highly dependent on the energy of a neutrino and its direction, the Gaussian energy PSF gets modified by a factor representing the effective area of the detector $A_{\mathrm{eff}}(E_i, \vec{x}_j)$. The new implemented effective areas are Zenith angle dependent. Plots of the new effective areas are shown in section 3.3.3 .

5.1.2 Background propability distribution function B_i

The background PDF is given by:

$$B_i = \frac{\sum_{j=1}^{N_{\mathrm{Bck}}} B_j(\vec{x}_i, \sigma_{\vec{x}_i}) \cdot \epsilon_j(E_i)}{N_{\mathrm{Bck}}}. \tag{5.1.11}$$

N_{Bck} denotes the number of randomised events which simulate background events in the detector. The direction of these background events are isotropically distributed over the whole sky. As all tested catalogs in this work do not take the galactic plane into account, the randomised maps show a stripe of $\pm 10\,\mathrm{deg}$ of galactic latitude removed.

The PSF $B_j(\vec{x}_i, \sigma_{\vec{x}_i})$ is defined analogous to the PSF factor in the signal term (eq. 5.1.6), as 1D Gaussian dependent on the angular distance of the random event position and the neutrino event position.

The energy PDF $\epsilon_j(E_i)$ is defined analogous to the energy PDF of the signal term in eq. 5.1.8.

5.2 Energy spectrum

Information for this chapter is taken from Spurio (2015) if not marked differently. Background in detectors like IceCube is mostly dominated by neutrinos and muons produced in showers induced by primary cosmic rays (CR) in the atmosphere.

The two principal chanels for production of atmospheric neutrinos and muons are the

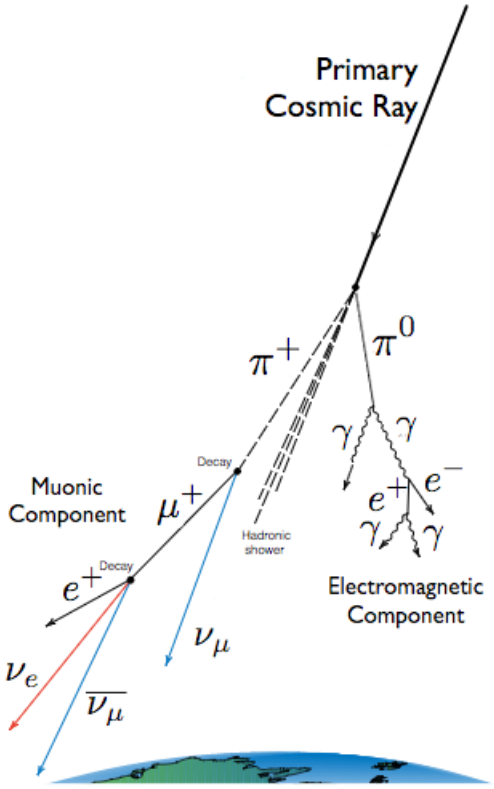

Figure 5.1: Schematic sketch of cosmic ray induced particle showers which occur as background in detectors like IceCube. Credit: Weaver (2015).

decays of charged mesons (pions and kaons):

$$\begin{aligned} \pi^+(K^+) &\rightarrow \nu_\mu + \mu^+ \\ \hookrightarrow \mu^+ &\rightarrow \bar{\nu}_\mu + \nu_e + e^+ \\ \pi^-(K^-) &\rightarrow \bar{\nu}_\mu + \mu^- \\ \hookrightarrow \mu^- &\rightarrow \nu_\mu + \bar{\nu}_e + e^- \end{aligned} \tag{5.2.1}$$

A schematic cosmic ray induced particle shower is shown in Figure 5.1. Figure 5.2 shows the differential cosmic ray flux, measured by different experiments. According to Beringer et al. (2012) the CR spectrum from several GeV to ultra-high energies is given by a power-law $E^{-\alpha}$ with differential spectral index of $\alpha = 2.7$. The primary CRs initiate particle showers in the atmosphere and produce secondary particles. According to Spurio (2015) these secondary particles can be described by a powerlaw again:

$$\frac{dN}{dE} \sim E^{-(\alpha+1)}. \tag{5.2.2}$$

Therefore the Monte-Carlo background is assumed to follow a power-law of the form $\frac{dN}{dE} \sim E^{-3.7}$.

Aartsen, Ackermann, et al. (2014) states a power-law spectral index for the detected neutrinos in the range from 2.0 to 2.3. Since the harder limit would eventuelly require a cut-off at PeV energies, the power-law $\frac{dN}{dE} \sim E^{-2.3}$ was chosen for a Monte-Carlo energy simulation for the sources. Figure 5.3 shows energy spectra created with Monte-Carlo simulations. The background spectrum with a spectral index of 3.7 is steeper than the signal spectrum with 2.3. Therefore restraining of potential background events in neutrino detectors is possible by making cut-offs for low energies.

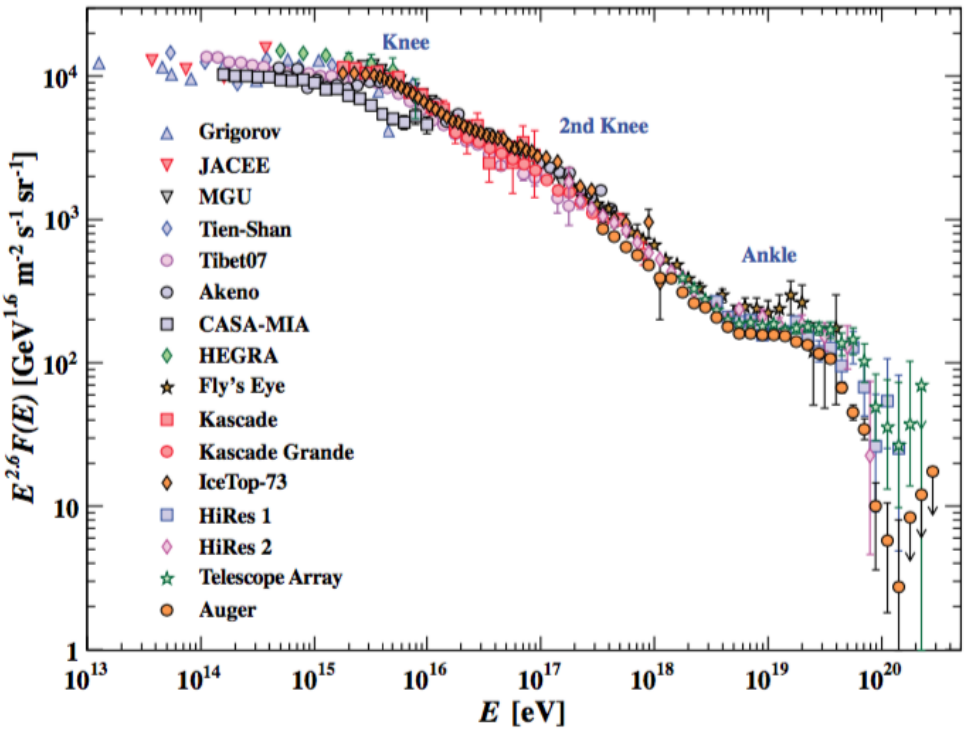

Figure 5.2: Differential CR flux $\Phi(E) \times E^{-2.6}$. Direct and indirect measurements of the CR flux by different experiments are listed in the legend. Credit: Beringer et al. (2012).

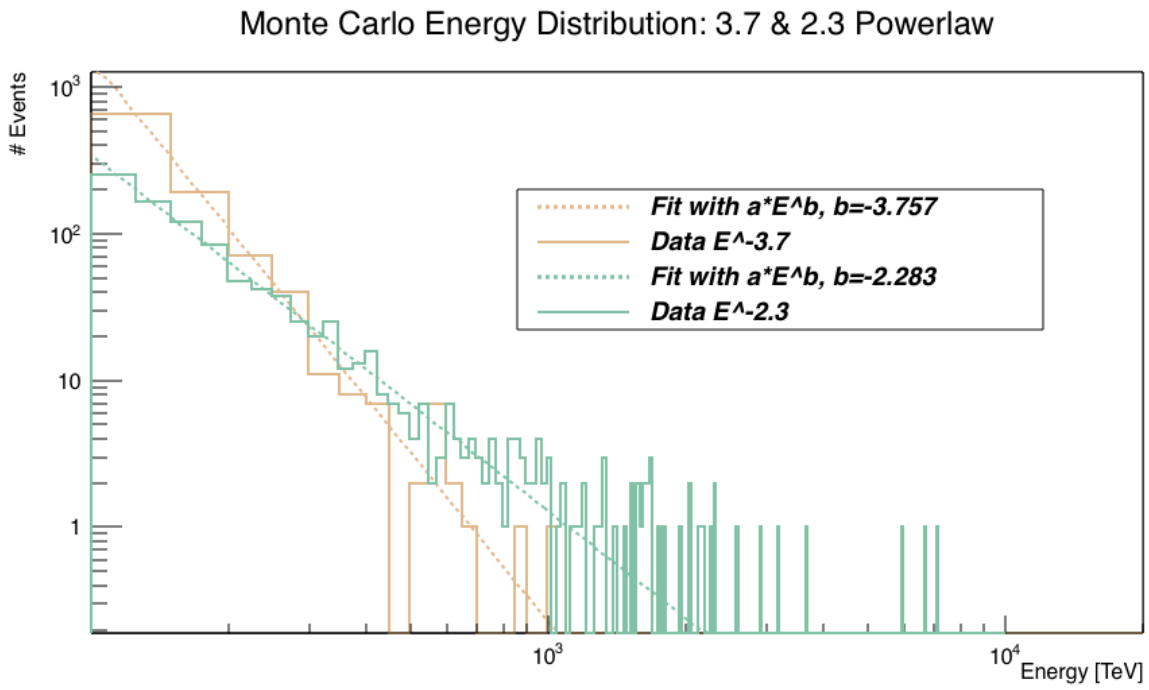

Figure 5.3: Monte-Carlo energy spectrum simulations with 1000 runs. The brown histogram shows the background spectrum with a powerlaw index of 3.7, the green histogram shows the signal energy distribution with an index of 2.3. The simulated data was fitted with powerlaws in the corresponding colors.

5.3 Test procedure

The likelihood algorithm described above produces likelihood curves like the one shown in Figure 5.4. The peak of this likelihood curve provides information about the correlation of the neutrino sample and tested catalogs. As the method is based on statistics, stable results can only be achieved by iteration of the calculations. In the end the calculated likelihood maxima of every iteration are filled in a histogram, like the one shown in Figure 5.5. The peak of the histogram is, depending on the number of iterations/runs, a relative stable value.

However, the position of this peak is strongly dependent on the size of the tested catalog, which is shown in Wiehl (2016). So far reductions of all tested catalogs to the size of the smallest catalog were necessary. This process can be done randomly or by selected parameters. In both cases the result strongly depends on the catalog size.

In order to compare different catalogs with varying sizes, the following test procedure was developed. At first 100 randomized catalogs with the size of the tested catalog are created. For this the galactic latitude of the sources in the tested catalog are reflected on the galactic plane. The galactic longitude is determined by random numbers.

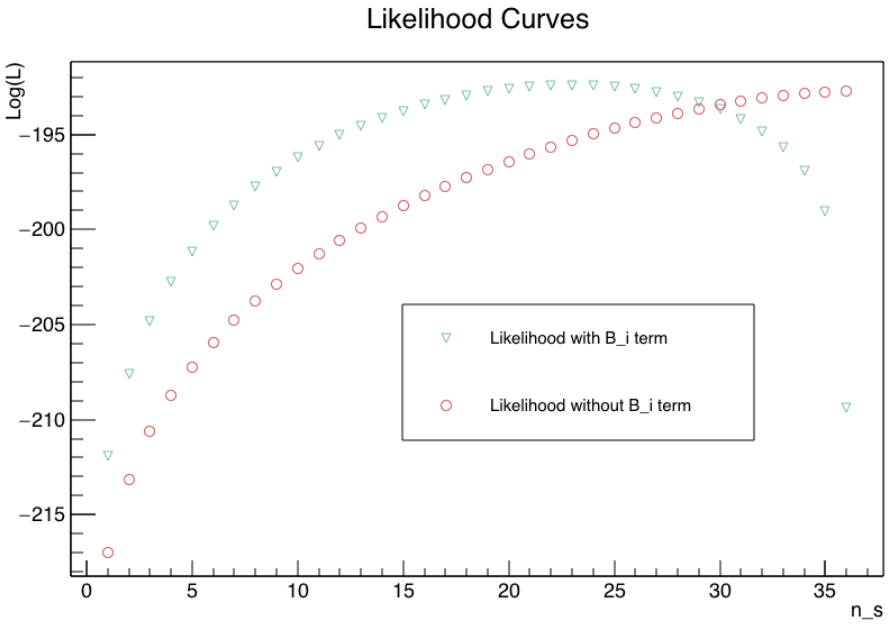

Figure 5.4: Plot of Log-Likelihoods with and with/without backgroundterm B_i. The Likelihood curve without background term has no maximum.

These 100 randomized catalogs are tested with 200 runs. Every histogram of these 100 tested radomized catalogs is fitted with a Gaussian. Afterwards the peaks of these 100 Gaussian histogram fits are applied in another histogram, like the one shown in figure 5.6. This histogram shows the distribution of random cataloges which is again Gaussian distributed

$$f(x) = a \cdot e^{-\frac{(x-\mu)^2}{2\sigma^2}}, \tag{5.3.1}$$

with the amplitude a, the position of the center μ and the standard deviation σ. The normalized amplitude will be denoted as $\hat{a}$. The actual catalog is tested with 10000 runs to achieve a very accurate result. The peak $\tilde{\mu}$ of the tested catalog is now drawn in the peak histogram of the randomized catalogs. The relative position of the tested catalog related to the random catalogs shows how much the tested catalog behaves like a random catalog. If the peak of the tested catalog is on the right side of the random catalogs it is better correlated than random catalogs, whereas a position left of the random catalog is worse. As the random catalogs are Gaussian distributed the correlation probability is the integral

$$p = \int_{\mu}^{\tilde{\mu}} 2\hat{a} \cdot e^{-\frac{(x-\mu)^2}{2\sigma^2}}, \tag{5.3.2}$$

after normalizing the Gaussian. Hereafter the probability will be positive for correlation ($\tilde{\mu} > \mu$) and negative for anticorrelation ($\tilde{\mu} < \mu$).

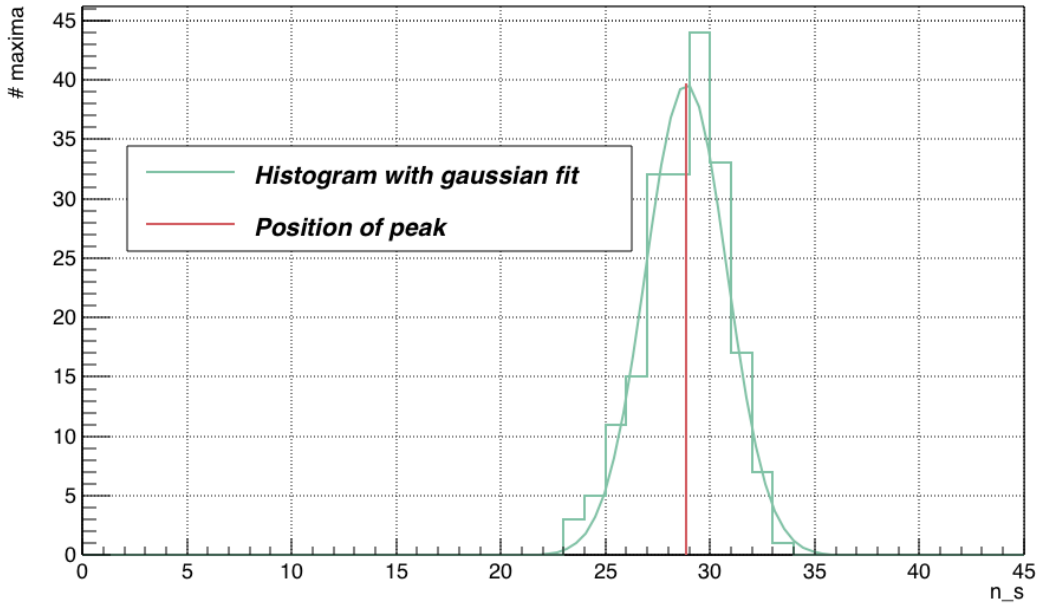

Figure 5.5: The likelihood curve peak of each run is filled in a histogram like the one shown here. The red line marks the peak of the gaussian fit of this histogram.

5.4 Neutrino events

The tests presented in this work use the High Energy Starting Events (HESE) sample published by Aartsen, Ackermann, et al. (2014). This sample contains 37 neutrino events measured in 988 days with energies up to 2 PeV. A list of all events can be found in Table 5.1. The IceCube Collaboration rejects a purely atmospheric explanation at $5.7\,\sigma$. The sample contains an estimated number of 8.4 ± 4.2 cosmic ray muon events and $6.6^{+5.9}_{-1.6}$ atmospheric neutrinos. Event 32 was caused by a coincident pair of background muons. This event is not considered in this work, due to missing energy and positional information. The angular errors are given as R_{50} radii, which means, that the event is observed with a propability of 50 % inside the corresponding circle. A skymap of the HESE events together with all source catalogs used for this work is shown in Figure 5.7.

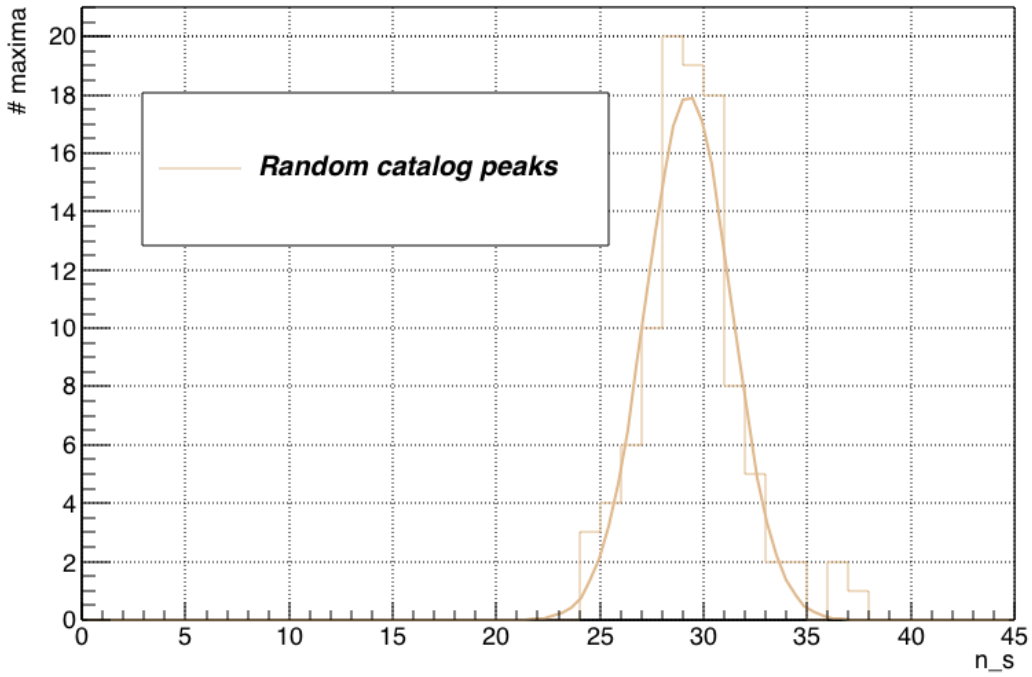

Figure 5.6: The peaks of the analysis procedure of 100 random catalogs are plotted in a histogram like the one shown here. This histogram is again Gaussian distributed.

5.5 Tested source catalogs

With the algorithm proposed here it is possible to test various source catalogs with any neutrino subsamples. An essential hypothesis of this work is the correlation of γ-ray flux of sources with their neutrino flux. Therefore, the tested catalogs were taken from the third catalog of active galactic nuclei detected by Fermi-LAT (3LAC) Ackermann et al. (2015). The catalog contains 1591 AGN located at high Galactic latitudes ($|b| > 10\,\mathrm{deg}$) detected between 100 MeV and 300 GeV. From this list of sources three different subsamples were built, a FSRQ sample (414 sources), a BL Lac sample (604 sources) and finally a BCU (blazar candidate of uncertain type, 404 sources) sample which includes not yet completely classified blazars. Figure 5.7 shows these three source catalogs together with the 36 used HESE events, plotted with their R_{50} radii.

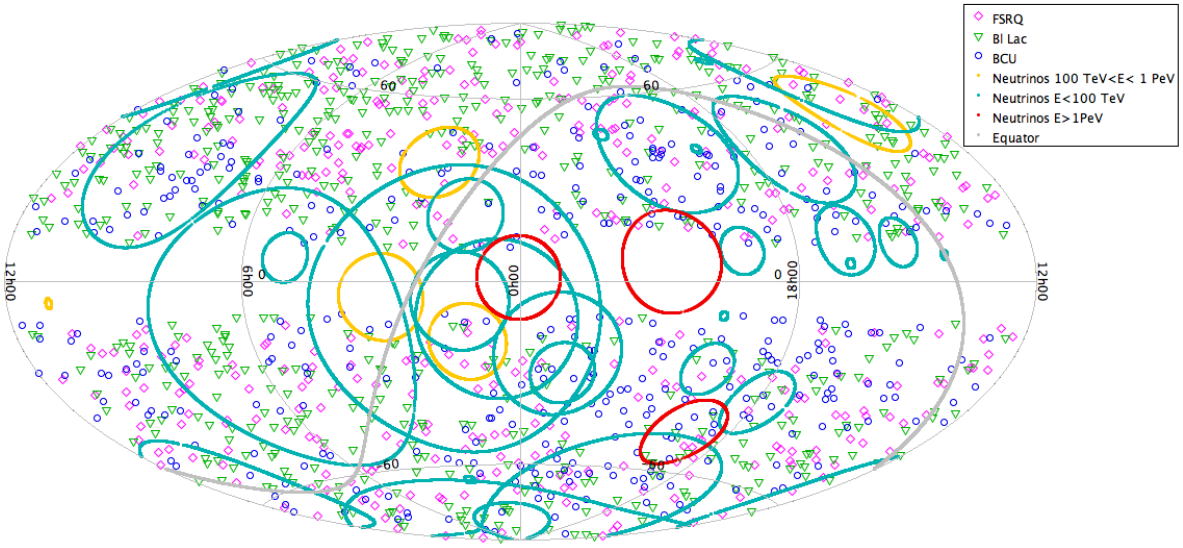

Figure 5.7: Sky map of all three 3LAC sub-catalogs tested in this work. The circles indicate the R_{50} radii of the 36 IceCube neutrinos.

Table 5.1: 37 HESE neutrino events of 988 days observation published by Aartsen, Ackermann, et al. (2014). Event 32 is not considered in this work, due to missing energy and position information.

ID	Energy [TeV]	Decl. [deg]	R.A. [deg]	Median angular error [deg]	Event Topology
1	$47.6^{+6.5}_{-5.4}$	-1.8	35.2	16.3	shower
2	117^{+15}_{-15}	-28.0	282.6	25.4	shower
3	$78.7^{+10.8}_{-8.7}$	-31.2	127.9	$\lesssim 1.4$	track
4	165^{+20}_{-15}	-51.2	169.5	7.1	shower
5	$71.4^{+9.0}_{-9.0}$	-0.4	110.6	$\lesssim 1.2$	track
6	$28.4^{+2.7}_{-2.5}$	-27.2	133.9	9.8	shower
7	$34.3^{+3.5}_{-4.3}$	-45.1	15.6	24.1	shower
8	$32.6^{+10.3}_{-11.1}$	-21.2	182.4	$\lesssim 1.3$	track
9	$63.2^{+7.1}_{-8.0}$	33.6	151.3	16.5	shower
10	$97.2^{+10.4}_{-12.4}$	-29.4	5.0	8.1	shower
11	$88.4^{+12.5}_{-10.7}$	-8.9	155.3	16.7	shower
12	104^{+13}_{+13}	-52.8	296.1	9.8	shower
13	253^{+26}_{-22}	40.3	67.9	$\lesssim 1.2$	track
14	1041^{+132}_{-144}	-27.9	265.6	13.2	shower
15	$57.5^{+8.3}_{-7.8}$	-49.7	287.3	19.7	shower
16	$30.6^{+3.6}_{-3.5}$	-22.6	192.1	19.4	shower
17	200^{+27}_{-27}	14.5	247.4	11.6	shower
18	$31.5^{+4.6}_{-3.3}$	-24.8	345.6	$\lesssim 1.3$	track
19	$71.5^{+7.0}_{-7.2}$	-59.7	76.9	9.7	shower
20	1141^{+143}_{-133}	-67.2	38.3	10.7	shower
21	$30.2^{+3.5}_{-3.3}$	-24.0	9.0	20.9	shower
22	220^{+21}_{-24}	-22.1	293.7	12.1	shower
23	$82.2^{+8.6}_{-8.4}$	-13.2	208.7	$\lesssim 1.9$	track
24	$30.5^{+3.2}_{-2.6}$	-15.1	282.2	15.5	shower
25	$33.5^{+4.9}_{-5.0}$	-14.5	286.0	46.3	shower
26	210^{+29}_{-26}	22.7	143.4	11.8	shower
27	$60.2^{+5.6}_{-5.6}$	-12.6	121.7	6.6	shower
28	$46.1^{+5.7}_{-4.4}$	-71.5	164.8	$\lesssim 1.3$	track
29	$32.7^{+3.2}_{-2.9}$	41.0	298.1	7.4	shower
30	129^{+14}_{-12}	-82.7	103.2	8.0	shower
31	$42.5^{+5.4}_{-5.7}$	78.3	146. 1	26.0	shower
32	-	-	-	-	coincident
33	385^{+46}_{-49}	7.8	292.5	13.5	shower
34	$42.1^{+6.5}_{-6.3}$	31.3	323.4	42.7	shower
35	2004^{+236}_{-262}	-55.8	208.4	15.9	shower
36	$28.9^{+3.0}_{-2.6}$	-3.0	257.7	11.7	shower
37	$30.8^{+3.3}_{-3.5}$	20.7	167.3	$\lesssim 1.2$	track

6 Results

The tests of this work were performed with the catalogs listed in chapter 5.5, which are FSRQ, Bl Lac and BCU. Additionally, a reference catalog (REF-Nu) was created. Basically it is a random catalog, like the ones used for calculation of the random peak histograms. The positions of 36 random sources of this catalog are replaced by the positions of the 36 HESE neutrino events. An appropriate test method should be able to distinguish such a perfect catalog from random catalogs.

The results of the calculations are presented in Table 6.1. A histogram of each tested catalog, together with a histogram of the tested catalog is shown in Figure 6.1. The red line indicates the peak of the Gaussian fit to the histogram of the tested catalog.

Among the tested subsamples FSRQs are by far the best correlated catalog. The catalogs BL Lac and BCU, however, show negative correlation propabilities. As described in section 5.3, negative correlation propabilities are possible. It means that a catalog lies left of the peak of the random catalog distribution (brown). So these two catalogs are less correlated than mean random catalogs. The correlation propability of the FSRQ subcatalog with a significance of $1.39\,\sigma$ is not high enough to be significant. If there is a correlation between tested FSRQs and the HESE events of this analysis, more neutrino events have to be included in the test in order to obtain significant results. However, the computed correlation propability could also be coincidental.

The REF-Nu catalog shows a strong correlation with a significance of almost 3 σ. This result shows, that the test procedure is able to detect a perfect catalog. However, the significance of the detection is still smaller than $5\,\sigma$. Real catalogs, containing neutrino emitting astrophysical objects, will never have the exact positions of the detected neutrinos. Furthermore, several neutrino events will be caused by background in the detector and therefore will not have astrophysical counterparts. Taking these effects into account, it is not possible to identify promising source candidates with the event samples used for this thesis.

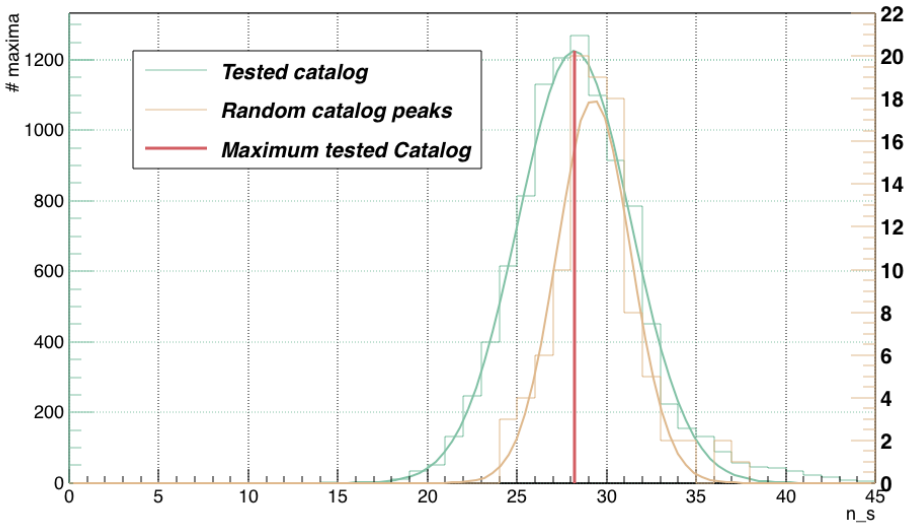
maxima
Tested catalog
Random catalog peaks
Maximum tested Catalog
n_s

(a) BCU

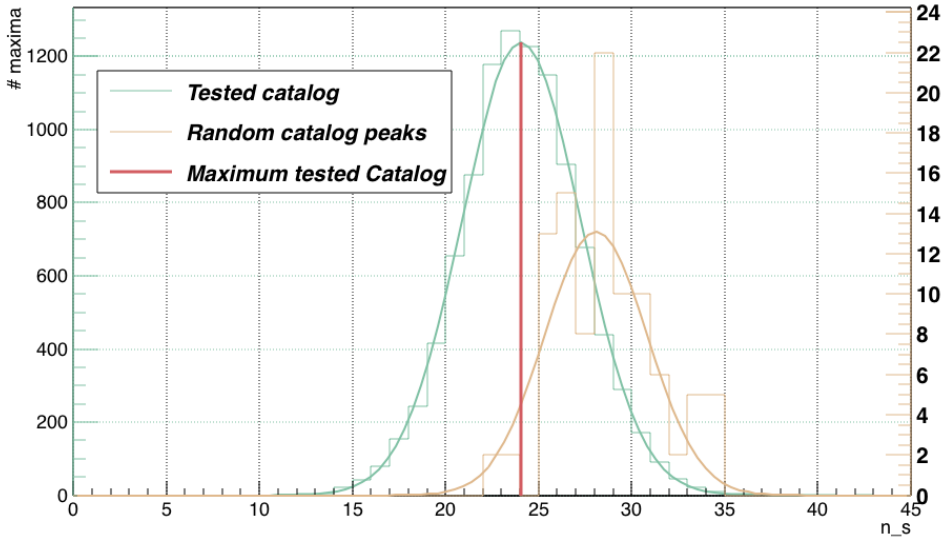
maxima
Tested catalog
Random catalog peaks
Maximum tested Catalog
n_s

(b) BL Lac

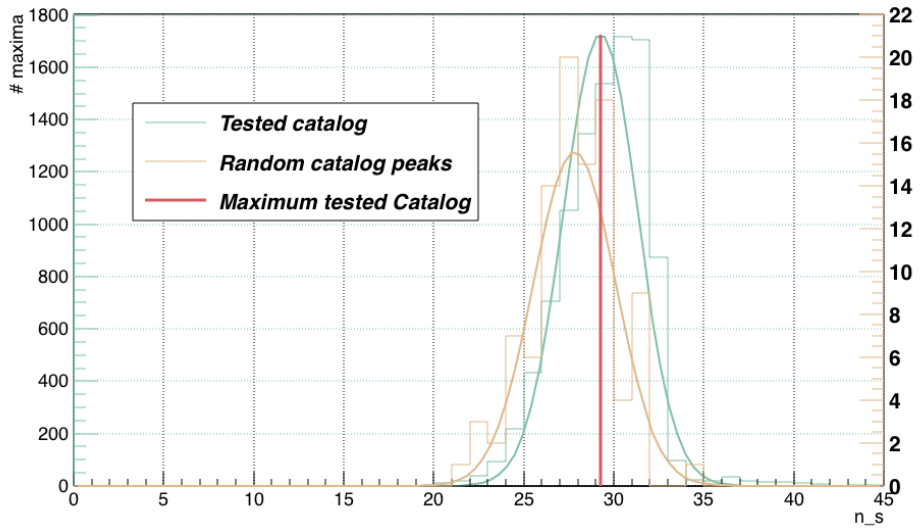

(c) FSRQ

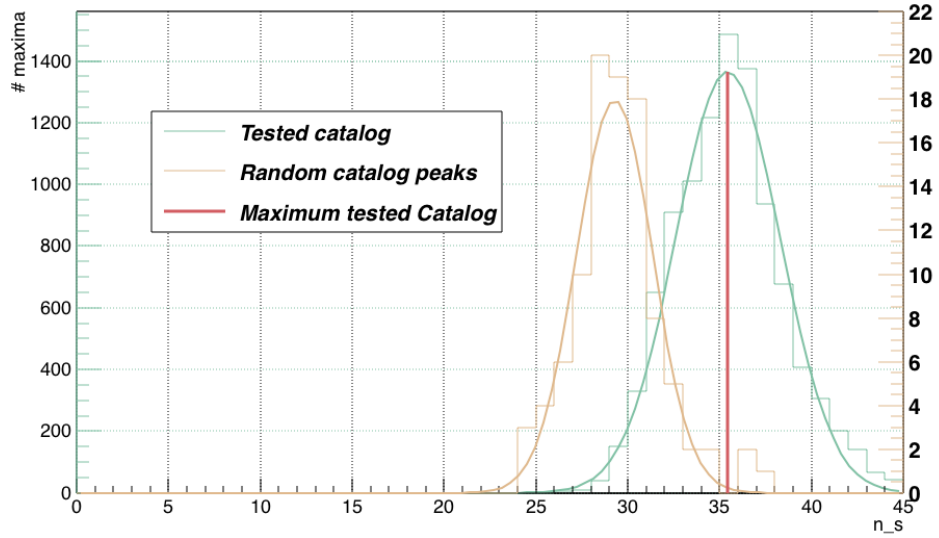

(d) REF-Nu

Figure 6.1: Graphical depiction of the final results of all four tested catalogs. The brown histogram with Gaussian fit shows the distribution of 100 peaks of calculated random catalogs. The green histogram is the calculated catalog, where the red line marks the position of the peak. If the red peak of a tested catalog is further right refered to the random distribution, it is stronger correlated.

Table 6.1: Results of the tests with 3 subsamples of the 3rd Fermi blazar catalog and a reference catalog(REF-Nu) with 36 inserted neutrino positions. Among the tested subsamples FSRQs are by far most correlated with the neutrino events. The REF-Nu, which contains all tested neutrino positions, shows a strong correlation with almost 3 σ.

Catalog	Probability p	Significance $[\sigma]$
FSRQ	0.475	0.64
BL Lac	-0.855	-1.46
BCU	-0.393	-0.51
REF-Nu	0.997	2.98

7 Summary and outlook

In this work a new statistical test method for correlation studies was developed. With this method it is possible to test the correlation of neutrino events with given catalogs of astronomical sources. The tests with subsamples of Fermi's 3rd catalog of blazars revealed a correlation of the IceCube HESE neutrino event sample and the FSRQ subsample with a significance of $1.39\,\sigma$. However, this result can still be coincidental. A test with an artificial REF-Nu catalog which consists of random source positions and the positions of the 36 neutrino events revealed, that the statistical method is able to recognize the correlation with a significance of $2.92\,\sigma$.

The results of this work show that the developed statistical method is able to find existing correlations between catalogs and neutrino event samples. However, the neutrino sample of the tests is still too small to produce results with significances $\geq 5\,\sigma$. In order to obtain enhanced results, larger neutrino samples are required. To reduce computation run times for the development of the test procedure of this work a neutrino sample with 36 events was used. At the moment IceCube already published event lists with 54 neutrino events of 4 years data-taking (Vincent et al., 2016). As IceCube is only running for some years now, more neutrino events can be expected in future. Furthermore, a secound km^3 neutrino detector Km3Net is constructed in the Mediteranean Sea at the moment (Margiotta, 2014). Additional data of this detector can be included.

On top of that, it is possible to use neutrino samples which contain only track events. These track events have much smaller directional uncertainties compared to shower events. This results in sharper distributions and therefore in clearer results, since the distance of a source to a event must be very small in order to obtain non-negligible correlation between this pair.

The structure of the test algorithms takes only the position and the flux of tested sources into account. This open structure allows tests for various kinds of sources. Besides active galactic nuclei there are further neutrino producing candidate source classes. Therefore, this method can be extended to other astronomical objects in future. Furthermore, tests of source classes, which are no neutrino candidates yet, could reveal interesting results.

8 Acknowledgements

Finally, I would like to express my gratitude to all people who helped and supported me during my bachelor thesis. Especially, I want to thank Prof. Dr. Karl Mannheim and Prof. Dr. Matthias Kadler for giving me the opportunity to work in this very interesting field of science. Their advice and the discussions in the weekly meetings taught me much, and made the time very inspiring and pleasant. Furthermore, my gratitude goes to Michael Kreter who was also member of these discussion meetings. He supported me with much enthusiasm whenever I needed additional advice. I want to thank him and also Dr. Dorit Glawion for proofreading my work and giving me numerous helpful remarks. Thanks to Juliane Wiehl for handing over a very clear commented c++ code and for the time spended to explain it to me. I would like to thank Marcus Langejahn for a very helpful introduction to TopCat.

Also, I want to thank the entire working group for the warm welcome. Special thanks to my office colleagues Michael Blank, Armar Hekalo, Stefan Lindeholz, Florian Rösch and Lukas Schrenk for the diverse discussions and the open atmosphere in our office. Moreover, thanks to my studies colleagues and good friends Michael Dahsler, Tobias Kuffer, Vladimir Markovic and Michael Seeg for the good time we had the last three years.

In the end I want to thank my family which always supports me and made all these experiences possible. I want to thank my love Laura especially for her understanding and support during and after my working hours.

Bibliography

Auffenberg, J. (2013). "IceTop as a veto in astrophysical neutrino searches for IceCube". *Proceedings, 33rd International Cosmic Ray Conference (ICRC2013): Rio de Janeiro, Brazil, July 2-9, 2013*, p. 0373. URL: http://www.cbpf.br/~icrc2013/papers/icrc2013-0373.pdf.

Aartsen, M. G., R. Abbasi, et al. (2014). "Energy reconstruction methods in the IceCube neutrino telescope". *Journal of Instrumentation* 9, P03009, P03009. DOI: 10.1088/1748-0221/9/03/P03009. arXiv: 1311.4767 [physics.ins-det].

Aartsen, M. G., M. Ackermann, et al. (2014). "Observation of High-Energy Astrophysical Neutrinos in Three Years of IceCube Data". *Physical Review Letters* 113.10, 101101, p. 101101. DOI: 10.1103/PhysRevLett.113.101101. arXiv: 1405.5303 [astro-ph.HE].

Abbasi, R., Y. Abdou, and T. Abu-Zayyad (2010). "Calibration and characterization of the IceCube photomultiplier tube". *Nuclear Instruments and Methods in Physics Research A* 618, pp. 139–152. DOI: 10.1016/j.nima.2010.03.102. arXiv: 1002.2442 [astro-ph.IM].

Abbasi, R., Y. Abdou, T. Abu-Zayyad, et al. (2012). "The design and performance of IceCube DeepCore". *Astroparticle Physics* 35, pp. 615–624. DOI: 10.1016/j.astropartphys.2012.01.004. arXiv: 1109.6096 [astro-ph.IM].

Abbasi, R., Y. Abdou, M. Ackermann, et al. (2013). "IceTop: The surface component of IceCube. The IceCube Collaboration". *Nuclear Instruments and Methods in Physics Research A* 700, pp. 188–220. DOI: 10.1016/j.nima.2012.10.067. arXiv: 1207.6326 [astro-ph.IM].

Ackermann, M. et al. (2015). "The Third Catalog of Active Galactic Nuclei Detected by the Fermi Large Area Telescope". *The Astrophysical Journal* 810, 14, p. 14. DOI: 10.1088/0004-637X/810/1/14. arXiv: 1501.06054 [astro-ph.HE].

Ahrens, J. et al. (2004). "Muon track reconstruction and data selection techniques in AMANDA". *Nuclear Instruments and Methods in Physics Research A* 524, pp. 169–194. DOI: 10.1016/j.nima.2004.01.065. eprint: astro-ph/0407044.

Beckmann, V. and C. Shrader (2012). *Active Galactic Nuclei*. Wiley-VCH.

Beringer, J. et al. (2012). "Review of Particle Physics*". *Phys. Rev. D* 86 (1), p. 010001. DOI: 10.1103/PhysRevD.86.010001. URL: http://link.aps.org/doi/10.1103/PhysRevD.86.010001.

Bleck-Neuhaus, J. (2013). *Elementare Teilchen: Von den Atomen über das Standard-Modell bis zum Higgs-Boson*. Springer Spektrum.

Blobel, V. and E. Lohrmann (1998). *Statistische und numerische Methoden der Datenanalyse*. Vieweg+Teubner Verlag.

Böttcher, M. et al. (2013). "Leptonic and Hadronic Modeling of Fermi-detected Blazars". *The Astrophysical Journal* 768, 54, p. 54. DOI: 10.1088/0004-637X/768/1/54. arXiv: 1304.0605 [astro-ph.HE].

Fermi, E. (1954). "Galactic Magnetic Fields and the Origin of Cosmic Radiation." *The Astrophysical Journal* 119, p. 1. DOI: 10.1086/145789.

Formaggio, J. A. and G. P. Zeller (2012). "From eV to EeV: Neutrino cross sections across energy scales". *Reviews of Modern Physics* 84, pp. 1307–1341. DOI: 10.1103/RevModPhys.84.1307. arXiv: 1305.7513 [hep-ex].

Gandhi, R. et al. (1996). "Ultrahigh-energy neutrino interactions". *Astroparticle Physics* 5, pp. 81–110. DOI: 10.1016/0927-6505(96)00008-4. eprint: hep-ph/9512364.

Gaskell, C. M. (2009). "What broad emission lines tell us about how active galactic nuclei work". *New Astronomy Reviews* 53, pp. 140–148. DOI: 10.1016/j.newar.2009.09.006. arXiv: 0908.0386.

Gasparrini, D. et al. (2015). "The 3rd Catalog of AGN Detected by the Fermi LAT". *ArXiv e-prints*. arXiv: 1508.05301 [astro-ph.HE].

Glüsenkamp, T. (2016). "Analysis of the cumulative neutrino flux from Fermi LAT blazar populations using 3 years of IceCube data". *European Physical Journal Web of Conferences*. Vol. 121. European Physical Journal Web of Conferences, p. 05006. DOI: 10.1051/epjconf/201612105006. arXiv: 1502.03104 [astro-ph.HE].

Gould, R. J. and G. Schréder (1966). "Opacity of the Universe to High-Energy Photons". *Phys. Rev. Lett.* 16 (6), pp. 252–254. DOI: 10.1103/PhysRevLett.16.252. URL: http://link.aps.org/doi/10.1103/PhysRevLett.16.252.

IceCube Collaboration (2016). *IceCube MasterClass*. URL: https://masterclass.icecube.wisc.edu/de.

IceCube-Gen2 Collaboration et al. (2014). "IceCube-Gen2: A Vision for the Future of Neutrino Astronomy in Antarctica". *ArXiv e-prints*. arXiv: 1412.5106 [astro-ph.HE].

Improved Reconstruction of Cascade-like Events in IceCube (2009).

Katz, U. F. and C. Spiering (2012). "High-energy neutrino astrophysics: Status and perspectives". *Progress in Particle and Nuclear Physics* 67, pp. 651–704. DOI: 10.1016/j.ppnp.2011.12.001. arXiv: 1111.0507 [astro-ph.HE].

Kowalski, M. P. (2004). "Search for Neutrino-Induced Cascades with the AMANDA-II Detector". PhD thesis. Humboldt-Universität zu Berlin.

Krawczynski, H. and E. Treister (2013). "Active galactic nuclei — the physics of individual sources and the cosmic history of formation and evolution". *Frontiers of Physics* 8, pp. 609–629. DOI: 10.1007/s11467-013-0310-3. arXiv: 1301.4179 [astro-ph.CO].

Longair, M. S. (2011). *High Energy Astrophysics*. Cambridge University Press.

Lovell, J. E. J. et al. (2008). "The Micro-Arcsecond Scintillation-Induced Variability (MASIV) Survey. II. The First Four Epochs". *The Astrophysical Journal* 689, 108-126, pp. 108–126. DOI: 10.1086/592485. arXiv: 0808.1140.

Mannheim, K. (1993). "The proton blazar". *Astronomy and Astrophysics* 269, pp. 67–76. eprint: astro-ph/9302006.

Margiotta, A. (2014). "The KM3NeT deep-sea neutrino telescope". *Nuclear Instruments and Methods in Physics Research A* 766, pp. 83–87. DOI: 10.1016/j.nima.2014.05.090. arXiv: 1408.1392 [astro-ph.IM].

Middell, E. (2008). "Reconstruction of Cascade-Like Events in IceCube". MA thesis. Humboldt-Universität zu Berlin.

Povh, B. et al. (2015). *Particles and Nuclei: An Introduction to the Physical Concepts*. Springer-Verlag Berlin Heidelberg.

Pucella, G. et al. (2008). "AGILE detection of intense gamma-ray emission from the blazar PKS 1510-089". *A&A* 491. Provided by the SAO/NASA Astrophysics Data System, pp. L21–L24. DOI: 10.1051/0004-6361:200810594. arXiv: 0810.1676. URL: http://adsabs.harvard.edu/abs/2008A&A...491L..21P.

Rädel, L. and C. Wiebusch (2012). "Calculation of the Cherenkov light yield from low energetic secondary particles accompanying high-energy muons in ice and water with Geant4 simulations". *Astroparticle Physics* 38, pp. 53–67. DOI: 10.1016/j.astropartphys.2012.09.008. arXiv: 1206.5530 [astro-ph.IM].

Rybicki, G. B. and A. P. Lightman (2004). *Radiative processes in astrophysics*. Wiley VCH.

Shakura, N. I. and R. A. Sunyaev (1973). "Black holes in binary systems. Observational appearance." *Astronomy and Astrophysics* 24, pp. 337–355.

Shields, G. A. (1978). "Thermal continuum from acretion disks in quasars". *Nature* 272, pp. 706–708. DOI: 10.1038/272706a0.

Spurio, M. (2015). *Particles and Astrophysics: A Multi-Messenger Approach*. Springer International Publishing.

Tavecchio, F. (2010). "Gamma-Ray Emission from AGNS (special Focus on BL Lac Objects)". *International Journal of Modern Physics D* 19, pp. 841–848. DOI: 10.1142/S0218271810017081. arXiv: 1001.4015 [astro-ph.HE].

The IceCube Collaboration (2008). "The IceCube Data Acquisition System: Signal Capture, Digitization, and Timestamping". *ArXiv e-prints*. arXiv: 0810.4930 [physics.ins-det].

Urry, C. M. and P. Padovani (1995). "Unified Schemes for Radio-Loud Active Galactic Nuclei". *Publications of the Astronomical Society of the Pacific* 107, p. 803. DOI: 10.1086/133630. eprint: astro-ph/9506063.

Vincent, A. C. et al. (2016). "Analysis of the 4-year IceCube HESE data". *ArXiv e-prints*. arXiv: 1605.01556 [astro-ph.HE].

Voigt, B. (2008). "Sensitivity of the IceCube Detector for Ultra-High Energy Electron-Neutrino Events". PhD thesis. Humboldt-Universität zu Berlin.

Wagner, S. J. and A. Witzel (1995). "Intraday Variability In Quasars and BL Lac Objects". *Annual Review of Astronomy and Astrophysics* 33, pp. 163–198. DOI: 10.1146/annurev.aa.33.090195.001115.

Weaver, C. (2015). "Evidence for Astrophysical Muon Neutrinos from the Northern Sky". PhD thesis. University of Wisconsin(Madison).

Wiehl, J. (2016). “Statistical analysis on the origin of the IceCube neutrino events”. MA thesis. Universität Würzburg.

Selbstständigkeitserklärung

Ich versichere, die vorliegende Arbeit selbstständig nach allgemeiner Studien- und Prüfungsordnung für die Bachelor- und Masterstudiengänge (ASPO) an der Julius-Maximilians-Universität Würzburg verfasst und keine anderen als die angegebenen Quellen und Hilfsmittel benutzt, sowie keiner anderen Prüfungsbehörde zur Erlangung eines akademischen Grades vorgelegt zu haben.

Würzburg, den 25. August 2016 Manuel Dörr